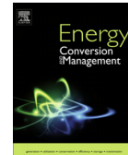




Contents lists available at ScienceDirect

## Energy Conversion and Management

journal homepage: [www.elsevier.com/locate/enconman](http://www.elsevier.com/locate/enconman)



# Integration of aero-elastic belt into the built environment for low-energy wind harnessing: current status and a case study

Angelo I Aquino<sup>\*1</sup>, John Kaiser Calautit<sup>2</sup>, Ben Richard Hughes<sup>1</sup>

<sup>1</sup>Department of Mechanical Engineering, University of Sheffield, Sheffield S10 2TN, UK

<sup>2</sup>Department of Architecture and Built Environment, University of Nottingham, NG7 2RD, UK

<sup>\*</sup>Corresponding author e-mail: [aiaquino1@sheffield.ac.uk](mailto:aiaquino1@sheffield.ac.uk)

## ABSTRACT

Low-powered devices are ubiquitous in this modern age especially their application in the urban and built environment. The myriad of low-energy applications extend from wireless sensors, data loggers, transmitters and other small-scale electronics. These devices which operate in the microWatt to milliWatt power range and will play a significant role in the future of smart cities providing power for extended operation with little or no battery dependence. Low energy harvesters such as the aero-elastic belt are suitable for integration with wireless sensors and other small-scale electronic devices and therefore there is a need for studying its optimal installation conditions. In this work, a case study presenting the Computational Fluid Dynamics modelling of a building integrated with aero-elastic belts (electromagnetic transduction type) was presented. The simulation used a gable-roof type building model with a 27° pitch obtained from the literature. The atmospheric boundary layer flow was employed for the simulation of the incident wind. The work investigates the effect of various wind speeds and aero-elastic belt locations on the performance of the device giving insight on the potential for integration of the harvester into the built environment.

The apex of the roof of the building yielded the highest power output for the aero-elastic belt due to flow speed-up maximisation in this region. This location produced the largest power output under the 45° angle of approach, generating an estimated 62.4 milliWatts of power under accelerated wind in belt position of up to 6.2 m/s. For wind velocity of 10 m/s, wind in this position accelerated up to approximately 14.4 m/s which is a 37.5% speed-up at the particular height. This occurred for an oncoming wind 30° relative to the building facade. For velocity equal to 4.7 m/s under 0° wind direction, airflows in facade edges were the fastest at 5.4 m/s indicating a 15% speed-up along the edges of the building.

## KEYWORDS

Aero-elastic flutter; Buildings; Computational Fluid Dynamics; Energy; Simulation; Aero-elastic belt

## 1. INTRODUCTION

The buildings sector demands 20 to 40% of total global power intake. This corresponds to values greater than the consumptions of industry and transport sectors [1]. Therefore new technologies that can mitigate or reduce the building energy demand are increasingly being developed; one of them is wind energy technology. One major benefit of building-integrated wind energy harvesting is bringing the power plant closer to the power consumers.

With the public having increased power creation capabilities, people can expect higher energy efficiency and reduced dependence to energy companies, lower carbon footprint and overall stimulation of the economy. Furthermore, it will decrease the load of the grid, dependence on diesel generators (in events of power outage) and more notably, lower transmission costs.

However, urban and suburban locations pose considerable problems for conventional mounted turbines. First is the significant turbulence in these areas, preventing the turbines from harnessing laminar wind flow. In these conditions wind turbine installers face deficiency in analysing the more complex wind conditions. This leads to the issues of unfavourable turbine site selection and therefore deficient power production.

Extreme vibration and noise generated by conventional wind turbine operation also present a great challenge in their integration into buildings. Another issue that rotational turbines face is the hazard of having blades fly off. These factors contribute to the anxiety of turbine installation among building owners and residents. But possibly the biggest challenge to the building-integrated wind turbine (BIWT) is its cost-effectiveness. Smaller wind turbines suitable for urban installations when fastened onto buildings have a high cost-to-energy-production ratio.

An emerging and novel alternative to the conventional turbines are wind-induced vibration energy harvesters. In recent years, low-energy power generation devices have been receiving increased attention due to their potential integration with self-powered micro-devices and wireless sensor networks in urban areas. Nano-generators have a wide span of potential power applications ranging from environmental and infrastructure monitoring, personal electronics to even wireless biosensing [3]. The power produced by these nano-generators is adequate to run light-emitting diodes [4], small liquid crystal displays [5] and self-powered wireless sensor nodes [3].

Such devices like the aero-elastic belt as shown in Figure 1 can be in a form of a small-scale wind generator that takes advantage of the flutter effect. Unlike turbine-based generators, the aero-elastic belt is a small-scale, light and inexpensive direct-conversion energy harvester which does not use any bearings, gears or rotors.

Fig 1. (a) Schematic diagram of an aero-elastic belt [6] (b) Example of experimental aero-elastic belt setup [7]

The standard rotating wind turbines mostly are not as effective when transformed into smaller types. However, flutter-based generators like the aero-elastic belt can be designed to fit lighter applications. It can operate in the range of microWatt to milliWatt power generation. Although the power output is low, it has its advantages compared to regular wind turbines. The aero-elastic belt is cost effective and can also be made of simple household materials. The device is small, compact, modular and suitable for turbulent flow, making it appropriate for integration with wireless sensors – an area which has the biggest application potential for this technology [8].

Current global demand for wireless sensors is increasing especially in applications of equipment supervision and monitoring revolving around energy expenditure, usage, storage and remote manipulation especially in the following areas:

- Medicine and health: prescription of patient-sensitive medications, remote monitoring and vital signs alerts
- Buildings: energy spending monitoring, security surveillance, structural health monitoring, damage detection
- Industry: systems tracking, data transfer, and equipment remote control
- Infrastructure & environment: traffic monitoring, indoor air safety levels, air and water pollution levels

These devices can be powered using low-energy generation technologies such as flutter and vibration harvesters. Figure 2 illustrates the wide array of applications that wireless sensors are operating in including, but not limited to, cities and urban environments. The primary obstacles to what is referred to as the “deploy-and-forget” quality of wireless sensor networks (WSN) are their limited power capacity and their batteries’ unreliable lifespans. To overcome these issues, low-energy harvesting of ambient energy resources like air flow, water flow, vibrations, and even radio waves has become an encouraging new field. Along with advancements in microelectronics, power requirements for wireless sensor nodes keep on dropping, ranging presently from microWatts to a few milliWatts [8].

Fig. 2. Applications of wireless sensors in smart cities [9]

The global market for energy harvesting devices and modules is growing with a forecasted increase in value from \$19 Million in 2012 to \$227 Million in 2017 – a 12-times increase in five years, with an annual growth of 51% per annum. It is important to mention that within the range of applications of energy harvesting devices, the buildings sector makes up the biggest portion of the market.

In 2011, there were more than 1 Million harvester modules sold across the world for building applications alone. This is due to the large network of wireless switches for lighting, air conditioning and sensors detecting occupants’ presence and measuring ambient room conditions such as humidity, all found in commercial buildings. Driving the market growth of energy harvesters are the large reduction in installation costs and maintenance-free operability requiring little or no wires [10]. Therefore, new

methods should be developed to further assess and optimised its integration with the built environment.

In this paper, the current status of vibration energy harvesting technologies, their scopes, advantages and limitations will be discussed followed by case study focusing on the analysis of the integration of an aero-elastic flutter technology into buildings using Computational Fluid Dynamics (CFD) modelling.

## 2. PREVIOUS RELATED WORK

In the following sections, different technologies that can harness flow induced vibration energy are examined.

### 2.1 Flow-induced vibrations

Aero-elastic flutter or simply referred to in this study as flutter, is a phenomenon of self-feeding oscillations upon which the aerodynamic forces on a structure associate with the inherent oscillation mode thereby producing fast recurring motion. Flutter can take place upon any body exposed to powerful steady fluid flow, under the precondition that a reinforcing feedback response ensues concerning the body's oscillation and the working fluid forces [8].

Flutter on itself can be severely catastrophic. Historic examples of flutter are the collapse of Tacoma Narrows Bridge and that of Brighton Chain Pier, as shown in Figure 3. The structures collapsed due to span failure caused by aero-elastic flutter [11]. Nevertheless, this seemingly violent nature of flutter can also be its source of strength when its potential for energy harnessing is explored.

Fig. 3. (a) A painting of the Brighton Chain Pier collapse in 1836 (b) A photo of the Tacoma Narrows bridge collapse in 1941 [11]

Flow-induced vibrations (FIV) is an umbrella category that includes flutter-induced vibrations or what the study will refer to as aero-elastic flutter or simply flutter, and vortex-induced vibrations [8].

#### 2.1.1 Extracted power and efficiency

For an incoming fluid flow, the energy that can be extracted is derived from the sum of two terms: the plunging term  $P_Y(t)$  and the pitching term  $P_\theta(t)$ :

$$P_\theta(t) = P_Y(t) + P_\theta(t) = F_Y(t) V_Y(t) + M(t) \omega(t) \quad (1)$$

where  $F_Y$  is the component of the force in the y-direction while  $M$  is the resulting torque relative to the pitching centre.

Instantaneous power can be expressed in nondimensional form as:

$$C_P = \frac{P}{\frac{1}{2}\rho U_\infty^3 c} \quad (2)$$

When integrated over one cycle, this instantaneous  $C_P$  gives the time-averaged power coefficient over one cycle called  $C_{Pmean}$ , given by the expression:

$$C_{Pmean} = C_{Phmean} + C_{P\theta mean} = \frac{1}{TU_\infty} \int_0^T [C_Y(t)V_Y(t) + C_M(t)\omega(t)]dt \quad (3)$$

where  $T$  is the period of oscillation,  $C_Y(t)$  is the instantaneous lift coefficient and  $C_M(t)$  is the momentum coefficient. These quantities are given in terms of  $\rho$ ,  $U_\infty$  and  $c$ :

$$C_Y(t) = F_Y(t) / \frac{1}{2}\rho U_\infty^2 c \quad (4)$$

$$C_M(t) = M(t) / \frac{1}{2}\rho U_\infty^2 c \quad (5)$$

The ratio of the average total power yield to the total power obtainable from the incoming airflow flowing across the swept region is defined as the power-extraction efficiency  $\eta$ :

$$\eta = \frac{P_{mean}}{\frac{1}{2}\rho U_\infty^3 A} = C_{Pmean} \frac{c}{A} \quad (6)$$

where  $A$  is the overall vertical distance of the movement of the aerofoil with both plunging and pitching motions being considered.

While it has been established that energy extracted from airflow originates from the sum of a plunging contribution  $C_{Ph}$  and a pitching contribution  $C_{P\theta}$ , for a foil with modified flapping motion the major source of extracted energy is through the plunging motion; the average extracted energy from the pitching motion is almost zero.

For a fixed pitching amplitude  $\theta_0$ ,  $C_{Pmean}$  increases with the reduced frequency  $k$  at first, then  $C_{Pmean}$  eventually decreases with the further increase in  $k$ . For every value of  $\theta_0$  there exists an optimal  $k$  for the maximum  $C_{Pmean}$ .

Similarly, for a fixed reduced frequency  $k$  this time, the same behaviour for  $C_{Pmean}$  can be noticed with respect to varying  $\theta_0$ . Due to their effects to the angle of attack,  $k$

and  $\theta_0$  were observed to affect the development of leading edge vortices (LEV) as well as changes in the lift coefficient  $C_L$ . It was also observed that high values for  $k$  and low values for  $\theta_0$  lead to higher plunging velocity  $V_\gamma$  and better synchronization between the lift coefficient and the plunging velocity compared to different scenarios. Concerning the amount of energy extracted, this is the best case. Therefore, to achieve the best performance for energy generation, relatively high  $k$  and low  $\theta_0$  are preferred [12].

## 2.2 Technologies

In this sub-section, three types of vibration energy harvesting technologies are reviewed; electromagnetic, piezoelectric and triboelectric devices.

### 2.2.1 Electromagnetic Vibration Devices

An example of an electromagnetic vibration device is the aero-elastic belt or also commonly known as the wind-belt, which is a small-scale wind generator that operates based on the phenomenon of aero-elastic flutter. The original invention puts the power production of wind-belts in the range from several milliWatts for the smallest-scale device to a 7.2 kWh device which is 1 m long operating in 6 m/s winds [13]. A significant upside is the production cost of such a low-power device could be very small as well.

In the study of Pimentel et al. [14], a wind-belt prototype was characterised. The device was 50-cm long and supported by a Plexiglass frame, with a tensioned Mylar membrane installed with bolts on its ends. This membrane had one side that is smooth and the other rough, thereby producing a simple aerofoil. The generator had an electromagnetic transducer incorporated in one end of the membrane. This transducer makes use of two small neodymium (NdFeB) magnets and a static coil positioned adjacent to the magnets. The wind flowing around the tensioned membrane caused it to flutter while the magnets vibrate relative to the coil, therefore inducing a current flowing in the coil, producing electric power as shown in the results in Figure 4. Based on the experimental results the minimum and maximum power output were: 5 milliWatts for airflow velocity equal to 3.6 m/s and load resistance of  $10 \Omega$  and 171 mW at 20 m/s,  $110 \Omega$  resistance and 38.1 N membrane tension.

Fig. 4. Power output for the wind-belt experimental test setup in [14]

Numerous parameters that affects the wind belt harvester's performance like the membrane tension, membrane length, magnet position and number of magnet were investigated by Arroyo et al. [13] using experimental testing. The study highlighted the optimal values for the key parameters, focusing on low wind speeds ranging from 1 to 10 m/s but with powerful vibration acceleration [13]. The experimental results

showing the amplitudes and frequencies for varying lengths of the ribbon used is shown in Figure 5.

Fig. 5. (a) Amplitude and (b) Frequency of vibration as a function of wind speed for various ribbon lengths [13]

Dinh Quy et al. [15] investigated a windbelt with the magnet mounted centrally along the flexible membrane made of a type of kite fabric called ripstop nylon fabric as shown in Figure 6. The single unit micro generator was able to produce power in the range of 3 - 5 mW. Five larger versions of these micro generators were combined to construct a windpanel, and together were able to generate 30 to 100 mW of power at wind speeds of less than 8 m/s. At low wind speeds between 3 to 6 m/s, the output current is approximately 0.2 to 0.5 mA, the generated voltage is between 2 to 2.5 V, and the generated power is about 2 to 3 mW, under membrane oscillation frequency of approximately 5 Hz.

Fig. 6. (a) 3D model of the wind belt design and (b) Fabricated test model studied in [15]

In Dinh Quy et al. [15] five of the single membrane generators were merged to fabricate a windpanel to increase the overall power output. The design of a single generator in this study was made in such a way that grouping can easily be constructed or dismantled. For each generator, two conducting coils of 4000 turns each were used and placed parallel to each other as shown in Figure 7.

Fig. 7. (a) The 3D model of the windpanel - a combination of five windbelts (b) Testing of the windpanel powering an LED light in actual wind conditions [15]

The earlier versions of flutter generators had practical problems as identified by Fei et al. [16]. One instance would be the physical contact of the vibrating membrane with the conductors once the membrane oscillation amplitude is greatest during strong winds. The positioning of the magnets fastened on the membrane must be carefully examined to guarantee optimised magnetic flux experienced by the conductors, which was also addressed by Dinh Quy et al. [15]. To tackle these problems and at the same time increase the efficiency of energy harvesting by a fluttering membrane, a novel variety of flutter-based-harvester was proposed in [16] which consists of a beam that acts as the support, an electromagnetic resonator, a power management circuit, a supercapacitor for storage of charge [16] and a spring. A thick polymer belt was used as the vibrating membrane having dimensions of 1 m by 25 mm by 0.2 mm. The electromagnetic resonator was positioned close to the end of the membrane. This was the preferred placement because of a higher bending stiffness of the membrane close to the secured ends. This configuration allowed a

heavier magnet to be supported by the vibrating membrane [16]. The supercapacitor is easily replaceable.

Dibin Zhu et al. [17] investigated a device with an aerofoil connected to a beam which was positioned after a bluff body as illustrated in Figure 8. This harvesting device operated at a relatively low wind velocity of 2.5 m/s and generated power equal to 470 microWatts. A disadvantage of this setup was requiring an initial displacement for the aerofoil in order to operate.

Fig. 8. (a) Schematic of energy harvester studied in [17] with measurements in mm  
(b) Experimental setup of the harvester (c) Operating principle of the energy harvester

Wang et al. [18] demonstrated a novel EMG-resonant-cavity wind generator integrated with dual-branch reed and tuning fork vibrator. The study highlighted the device's magnetic circuit being able to intensify the rate of change of the time-varying magnetic flux. The tuning-fork assembly of the device was able to further decrease system losses. Peak power output was observed to be 56 mW for airflow speed equal to 20.3 m/s with corresponding conversion efficiency of 2.3% at airflow speed of 4 m/s. The experiments provided evidence that the device can operate in a large range of wind speeds. The diagrams and working process of this wind energy harvester are shown in Figure 9.

Fig. 9. (a) Output voltage vs. coil position [18] (b) Wind speed vs. max output power and efficiency (c) Working process of electromagnetic energy harvester [18]

Kim et al. [19] investigated two types of electromagnetic energy harvesters that utilise direct airflow power conversion to mechanical oscillations - (i) a wind-belt-like oscillatory linear energy harvester specifically for powerful air streams and (ii) a harvester centred on a *Helmholtz resonator* concentrated on sifting energy from weaker air current such as environmental air streams. The proposed wind-belt-like energy harvester was centred on the principle of aero-elastic flutter effect. It was composed of a polymer resonator together with entrenched magnets, a polymer casing and copper coils. The moving part of the generator was made up of an oscillating membrane with fastened permanent magnets, placed in the centre of the flow passage. The device casing had an inlet and an outlet for the airflow. The peak-to-peak open-circuit voltage for two types of belt materials, Mylar and Kapton, are shown in Figure 10 (a), while output voltage was measured for different airflow strengths shown in Figure 10 (b).

Fig. 10. (a) Measured peak-to-peak open-circuit voltage while varying input pressure  
(b) Output voltage in coil measured under weak and strong wind [19]

The second energy harvester made use of a Helmholtz resonator as a mechanism to concentrate oncoming wind flow. In simple terms, a Helmholtz resonator has a chamber filled with air, with an unconstrained neck, in which an ordinary fluid oscillation takes place. Being a resonator, the air within the neck serves as the oscillating weight while air within the air chamber serves as the elastic mechanism. Figure 11 displays the operating principle for this energy harvester. This harvester is claimed to be able to operate in extremely slow flows.

The wind-belt-like oscillatory energy harvester offered a peak to peak amplitude AC voltage equivalent to 81 mV at frequency of 0.53 kHz, generating from an input of 50 kPa of pressure. The Helmholtz-resonator-centred generator reached a peak to peak amplitude AC voltage of 4 mV at frequency of 1.4 kHz, from 0.2 kPa pressure input, corresponding to 5 m/s or 10 mph wind speeds.

Fig. 11. Schematic plan illustrating the principle of operation of energy harvester in [19]: (a) at rest state; (b) at resonance through wind flow.

Munaz et al. [20] demonstrated that there was potential for the power generation of the electromagnetic energy harvester via vibrations to be amplified many times over by the introduction of several magnets as the moving mass even if all other experimental variables were fixed. The device generated 224.72  $\mu$ W in DC power, having 200  $\Omega$  load resistance for a 5-magnet system. This device operates at a subtle resonance frequency equivalent to 6 Hz, which was deemed appropriate for handheld devices and remote sensing applications.

Wang et al. [21] discussed a study on energy harvesting through vibrations caused by the Karman vortex street through an electromagnetic harvester producing instantaneous power of 1.77  $\mu$ W under exposure to the vortex street. Figure 12 shows the measured displacement history and the open circuit voltage induced by the coil which measured approximately 20 mV peak-to-peak. In the same study it was stated that the vibrations can also be harnessed from other fluid flow - river streams, tire air pressure flow or fluids in mechanical equipment.

Fig. 12. (a) Magnet displacement and (b) Induced voltage by the coil for a typical cycle [21]

### 2.2.2 Piezoelectric Energy Harvesting Devices

Demori et al. [22] explored a piezoelectric energy harvesting illustrated in Figure 13 (a) where a stepper motor is attached to a piezoelectric converter that can vary the beam angle relative to the flow. The output of the energy harvesting system together with its power conditioning circuit was tested through measurements of the transmission time versus flow. A peak power of 100  $\mu$ W was collected and

transmission time of 2 s was measured. A retransmission interval under 2 minutes was attained. It was noticed that for this system, the highest output was achieved around flow velocity of 4 m/s, as shown in Figure 13 (b).

Fig. 13. (a) Piezoelectric energy harvesting system schematic (b) Average power output and retransmission time interval as a function of air flow velocity [22]

Shan et al. [23] studied a macrofiber composite piezoelectric energy harvesting device for water vortex, which generated 1.32  $\mu\text{W}$  power output under liquid water flow speed of 0.5 m/s, showing the plausibility of using this harvesting technology for liquid flow as well. Weinstein et al. [24] investigated power from a piezoelectric shaft influenced by vortex shedding from a bluff cylinder, which generated 200  $\mu\text{W}$  and 3 mW of power at air velocities of 3 m/s and 5 m/s.

Li et al. [25] investigated a piezoelectric energy harvesting device which used flexible piezoelectric materials as “stalks” together with polymer membrane acting as leaf-like structures. The experiment result confirmed a maximum power output of 615  $\mu\text{W}$  for an airflow speed of 8 m/s and 5  $\text{M}\Omega$  resistance while using a two-layer stalk. The maximum power density was 2036  $\mu\text{W}/\text{cm}^3$  for a single leaf. Furthermore, the work noted that their energy harvesters demonstrated good power performance normalized by volume, mass and expenditure. Although their harvesters performed were not effective in terms of power per swept-area. The study recommended that the swept-area performance could be enhanced through assembling multiple harvesters behind one another. Figure 14 shows the performance of the piezo-leaf where in (b) different shapes of the leaf were tested including square, round, isosceles triangle with  $30^\circ$  base angle, isosceles triangle with  $45^\circ$  base angle, equilateral triangle, and rectangle (Sq, Ro, T30, T45, T60 and Re, respectively)

Fig. 14. (a) Wind response of piezo-leaf with varying wind speeds (b) Power output of the different shapes of piezo-leaf [25]

St. Clair et al. [26] investigated a micro-generator that utilised flow-generated self-excited fluctuations. This concept was analogous to a musical harmonica that produces sounds through vibrations of its reeds when fluid is blown. This device performed with an power generation from 0.1 to 0.8 mW while operating at airflow speeds spanning between 7.5 and 12.5 m/s. Figure 15 shows the general working principle of the device and the maximum power output as a function of air pressure for two types of beams (Aluminium and Steel) where the curves represent simulation results and the dots indicate experimental results.

Fig. 15. (a) Piezoelectric energy harvester utilising flow-induced oscillations (b) Maximum power output as function of air pressure for two beam types – Aluminium and Steel [26]

Erturk et al. [27] examined the concept of piezo-aero-elasticity for energy harvesting using a mathematical model and experiments. The harvester has a 50 cm long aerofoil that is vertically oriented. Two piezoceramics of type Lead Zirconate Titanate-5A (PZT-5A) were fastened to two extremities of the aerofoil. Upon interacting with air, the aerofoil moves and triggers the piezoceramics thereby generating electric current. The results showed 10.7 mW of power yield for 9.3 m/s flutter velocity using a resistive load of 100 k $\Omega$  load.

Dickson [28] developed a novel deployable flutter energy harvester based on a structure resembling a tree composed of several “leaves” of piezoelectric devices. Preliminary experiments demonstrated that power output by the cylinders was low mainly due to the quality and dimensions of chosen piezoelectric materials. Yet there were results referred to from Bryant et al. [29] and McCarthy et al. [30] that showed that there was an optimum spacing for the tandem of devices that triggered trailing cylindrical energy harvesters to generate appreciably greater energy compared to the leading harvester. It is noteworthy that this finding was in contrast to that of conventional horizontal axis wind-turbines (HAWTs), for which tandem orientations generally avoided because to energy harvesting shortfalls in wakes areas shown by Burton et al. [31]. Figure 16 shows the leaf-type harvester with its performance under smooth and turbulent airflows.

Fig. 16. (a) The Polyvinylidene-fluoride (PVDF) [28] leaf; and (b) Harvester’s voltage spectral density for smooth and turbulent wind flow of 8 m/s at 135° flow angle [32]

The “tree” concept was tested by Li et al. [33]. This harvester with leaves made of Polyvinylidene-fluoride (PVDF) was subjected to wind speeds from 3 to 8 m/s. The leaves are triangular in shape. It was earlier discovered in [25] that the triangular shape provided the highest power output among several different tested shapes. It was also found out that the energy harvester functioned best when it has flutter oscillations under the Limit-Cycle Oscillations (LCOs) as opposed to chaotic flutter [34]. An electroactive area power density,  $P_{EAA} \leq 45 \mu W/cm^2$  was attained [25] by the piezoelectric tree, where it was shown in [39] that 296  $\mu W$  peak power was harnessed at top speed of 8 m/s.

Hobbs and Hu [35] developed energy harvesters based on rounded cylinders which were positioned in groupings at different spacings subject to wind tunnel flow as shown in Figure 17. These cylinders were fastened to piezoelectric discs close to the bottom and were allowed to oscillate in the cross-stream direction.

Fig. 17. (a) Experimental setup and (b) schematic diagram of parallel circular cylinders studied by [35]

Hobeck and Inman [36] examined energy harvester called “piezoelectric grass”. In this investigation, several piezoelectric ceramic materials made of PZT were configured such that there were bending oscillations in the structure near-wake flow. Power output of 1 mW per PZT beam was attained for a flow speed of about 11.5 m/s, and it was also discovered that optimum turbulence conditions could maximised the power output. Figure 18 shows how the average power output is related to the position of the harvester with respect to the bluff body and the velocity of airflow for two types of harvester arrays – PVDF and PZT. The PZT type generates higher power output per element in the milliWatt range, as mentioned earlier.

Fig. 18. Power output with varying flow velocity and bluff body position for (a) PVDF harvester array, and (b) PZT harvester array [36]

Akaydin et al. [37] investigated energy harvesting system based on piezoelectric shaft along the trail of a round cylinder subjected to unsteady wind flow. As illustrated in Figure 19 (d), the shaft is configured to be parallel with respect to the oncoming wind and was held secured at the downstream edge. The study showed that the gap between the vortices’ circulation and the vortices distance from the shaft had influence on the output power was. The greatest power was around 4  $\mu$ W with Reynolds number of approximately 14800 at the shaft’s resonant frequency.

A known mechanism for boosting pressure variation amplitudes occurring in a vortex street was to utilise an array of structures in group configuration as shown in Figure 19 (f). [38] and [39] both stated that two bluff structures in arranged in such a way could increase the hydrodynamic oscillations created by the phenomenon of vortex shedding. Consistency of the vortices was also enhanced when two bluff structures were present instead of a single one [40].

Fig. 19. Schematic diagrams showing different energy harvesting devices presented in (a) [41]; (b) [42]; (c) [43]; (d) [37]; (e) [17]; (f) [38]

Song et al. [44] investigated a piezoelectric device based on composite cantilever immersed in water instead of air illustrated in Figure 20. Highest power output of the harvester was observed to be 21.86  $\mu$ W which was attained at a water flow of 0.31 m/s.

Fig. 20. (a) Schematic diagram; (b) x-y planar diagram; and generated power as function of water velocity with varying cylinder diameters for (c) upstream beam (d) downstream beam [44]

Matova et al. [45] described an energy harvester containing an enclosed piezoelectric device inside a *Helmholtz resonator*, as shown in Figure 21 (a). It was discovered in the study that enclosed harvesters performed better than exposed

harvesters because the enclosure negated the viscous effect of air within the Helmholtz cavity and guaranteed that only the fluctuation stimulated the harvester. Tests revealed that the energy harvester produced a peak power of 2  $\mu\text{W}$  subjected to air flow speed of 13 m/s at a frequency of 309 Hz. However, a disadvantage of the Helmholtz resonator was its resonant frequency's dependence to the surrounding temperature. This entailed that this type of harvester could only be utilised in settings with steady temperature ranges, otherwise the harvester must be redesigned to operate at a wider frequency range. Figure 21 (b) shows the generated power of the harvester for a constant flow velocity of 14 m/s and load resistance of 3.3  $\text{M}\Omega$  with varying cavity volume of the Helmholtz resonator.

Fig. 21. (a) Helmholtz resonator with piezoelectric energy harvester (b) Power output of harvester for airflow of 14 m/s with resistance of 3.3  $\text{M}\Omega$  [45]

### 2.2.3 Triboelectric and Hybrid Generators

Xie et al. [46] proposed *triboelectric nanogenerator* (TENG) that was able to harvest miniature wind energy ambient in normal human habitats developed utilising common materials. This system had a rotating part that enabled the sweeping motion of several triboelectric films called polytetrafluoroethylene (PTFE), thereby making alternating contact and separation with Aluminium sheets. This process of cyclical physical contact and disconnection between distinct planes with opposing triboelectric charges was responsible for generating an induced voltage across two electrodes, therefore pushing flow of electrons in an alternating current. This particular rotary triboelectric nanogenerator (R-TENG) was able to achieve a peak power of 62.5 mW, a peak power density of about 39  $\text{W}/\text{m}^2$  at airflow speeds of around 15 m/s, from approximately 250 V open-circuit voltage with a 0.25 mA short-circuit current. This investigation had shown that triboelectric nanogenerators could work hand-in-hand with wind power.

Liang et al. [47] investigated a *multi-unit transparent triboelectric nanogenerator* (MT-TENG), which is intended to harvest energy from ambient water movements like rain water as illustrated in Figure 22. The peak instantaneous power density was measured at 27.86  $\text{mW}/\text{m}^2$ . This value is 11.6 times larger than the output of a single transparent TENG of the same operating size.

Fig. 22. Working mechanism leading to the improved efficiency of the MT-TENG; inset shows potential application in buildings [47]

Bae et al. [48] studied a flutter-based wind harvesting triboelectric generator. This flutter-driven triboelectric generator (FTEG) is relatively small being only 7.5 cm long and 5 cm wide. Nevertheless it demonstrated instantaneous outputs of approximately 200 V and current of 60  $\mu\text{A}$  under 15 m/s wind speeds equivalent to 158 Hz. This corresponds to 0.86 mW of output power. The authors also characterised the

generator by its different modes of operation based on its components' contact type. There are three modes they discovered: single, double and chaotic. The transitions between modes are shown in Figure 23, wherein the transition from single to double-contact mode ensues corresponding to decreasing mass ratio.

Fig. 23. Velocity vs. mass ratio plot of the relationship between flag and plate behaviour showing the different contact modes [48].

## 2.3 Challenges

Previous studies about the building environment's potential for wind energy harvesting highlighted the need for detailed and accurate analysis of wind flow around buildings. To utilise the effect of wind acceleration above or around buildings and to be able to determine the appropriate type of wind energy technology to be installed sufficient integration analysis has to be conducted. In addition, there is the challenge to analyse optimum position of the wind energy harvesters. Accurate simulations will lead to more information that can result to better decisions [2].

No previous work studied the integration of low-energy vibration harvesting devices in buildings or structures. Most studies for these energy harvesters are carried out in laboratory settings. There is also a lack in numerical studies about these energy technologies. There is a lack in research about the applications of these harvesters in the urban environment. Most theoretical works use unrealistic boundary conditions like the utilisation of uniform flow. Currently very few studies were done involving actual field tests with real-world conditions. If low-energy harvesters are to become widely commercial, field tests observable by the public need to be increased. This study will address this by carrying out an urban flow simulation of a small building integrated with low-energy harvesters and assess the impact of varying outdoor wind conditions.

## 3. CASE STUDY: ANALYSIS OF THE INTEGRATION WITH THE BUILT ENVIRONMENT

The work will investigate the effect of various external conditions and device locations on the performance of the aero elastic belt. The simulation will use a gable-roof type building model with a 27° pitch as shown in Figure 24. The atmospheric boundary layer (ABL) flow will be used for the simulation of the approach wind. The three-dimensional Reynolds-averaged Navier-Stokes (RANS) equations together with the continuity and momentum equations will be solved using ANSYS FLUENT 16 for obtaining the velocity field and also pressure field. Sensitivity analyses for the CFD grid resolutions will be executed for verification of modelling. In addition, the results of the flow around the buildings and surface pressure coefficients will be validated with previous experimental work. The study will utilise regression analysis and experimental data [6] to estimate the power output of the aero-elastic belt. The coil used in the transducer are composed of 38 American wire gauge (awg)

enamelled wire with 150 turns and approximately 25 ohms internal resistance [49]. Figure 24 shows the location of the aero elastic belt around the building geometry.

Fig. 24. CAD geometry of building with aero-elastic belt devices

### 3.1 Computational Fluid Dynamics modelling

The fundamental assumptions for the numerical simulation involve a 3D, fully turbulent, and incompressible flow. The flow was modelled by making use of the standard k- $\epsilon$  turbulence model, which is a well-established research technique regarding airflows surrounding buildings [50]. The Finite Volume Method (FVM) was utilised with the CFD model together with the Semi-Implicit Method for Pressure-Linked Equations (SIMPLE) velocity and pressure coupling algorithm using the second order upwind discretisation. The governing equations are the continuity equation (Eqn. 7), momentum equation (Eqn. 8) and energy equation (Eqn. 9). The standard k- $\epsilon$  transport model was employed to classify the turbulence kinetic energy and flow dissipation rate within the simulation model. The transport equations are shown in Eqn. 10 and Eqn. 11.

$$\frac{\partial}{\partial t}(\alpha_q \rho_q) + \nabla \cdot (\alpha_q \rho_q \vec{v}_q) = \sum_{p=1}^n (\dot{m}_{pq} - \dot{m}_{qp}) + S_q \quad (7)$$

$$\frac{\partial}{\partial t}(\alpha_q \rho_q \vec{v}_q) + \nabla \cdot (\alpha_q \rho_q \vec{v}_q \vec{v}_q) = -\alpha_q \nabla p + \nabla \cdot \bar{\tau}_q + \alpha_q \rho_q \vec{g} + \sum_{p=1}^n (\vec{R}_{pq} + \dot{m}_{pq} \vec{v}_{pq} - \dot{m}_{qp} \vec{v}_{qp}) + (\vec{F}_q + \vec{F}_{\text{lift},q} + \vec{F}_{\text{vm},q}) \quad (8)$$

$$\frac{\partial}{\partial t}(\alpha_q \rho_q h_q) + \nabla \cdot (\alpha_q \rho_q \vec{u}_q h_q) = \alpha_q \frac{\partial p_q}{\partial t} + \bar{\tau}_q : \nabla \vec{u}_q - \nabla \cdot \vec{q}_q + S_q + \sum_{p=1}^n (Q_{pq} + \dot{m}_{pq} h_{pq} - \dot{m}_{qp} h_{qp}) \quad (9)$$

where;  $\vec{v}_q$  denotes the velocity of phase q and  $\dot{m}_{pq}$  and  $\dot{m}_{qp}$  characterizes the mass transfer from the pth to qth phase and vice-versa.  $\bar{\tau}_q$  denotes the qth phase stress-strain tensor.  $h_q$  denotes the specific enthalpy of the qth phase and  $\vec{q}_q$  denotes the heat flux.  $Q_{pq}$  is the heat exchange intensity between the pth and qth phases and  $h_{pq}$  is the interface enthalpy.  $S_q$  denotes the source term.

$$\frac{\partial}{\partial t}(pk) + \frac{\partial}{\partial x_i}(\rho k u_i) = \frac{\partial}{\partial x_j} \left[ \left( \mu + \frac{\mu_t}{\sigma_k} \right) \frac{\partial k}{\partial x_j} \right] + G_k + G_b - \rho \epsilon - Y_M + S_k \quad (10)$$

$$\frac{\partial}{\partial t}(\rho \epsilon) + \frac{\partial}{\partial x_i}(\rho \epsilon u_i) = \frac{\partial}{\partial x_j} \left[ \left( \mu + \frac{\mu_t}{\sigma_e} \right) \frac{\partial \epsilon}{\partial x_j} \right] + C_{1\epsilon} \frac{\epsilon}{k} (G_k + C_{3\epsilon} G_b) - C_{2\epsilon} \rho \frac{\epsilon^2}{k} + S_\epsilon \quad (11)$$

where;  $G_k$  denotes turbulence kinetic energy generation due to the mean velocity gradients,  $G_b$  denotes turbulence kinetic energy generation due to buoyancy.  $Y_M$  denotes the contribution of fluctuating dilatation in compressible turbulence to the overall dissipation rate.  $C_{1\epsilon}$ ,  $C_{2\epsilon}$  and  $C_{3\epsilon}$  are constants,  $\sigma_k$  and  $\sigma_e$  are the turbulent Prandtl numbers for k and  $\epsilon$ .  $S_k$  and  $S_\epsilon$  are the source terms.

The geometry (Figure 25) was designed making use of an academic standard CAD tool and then exported into ANSYS Geometry to generate a computational model. The shape of the building was based on [51], which is a gable roof type building with a roof pitch of 26.6°. The overall dimension of the building was 3.3m (L) x 3.3m (W) x 3m (H). The fluid volume was isolated from the solid model to generate a computational domain. The fluid domain contained an inlet on one side of the domain, and an outlet on the opposite boundary wall.

The COST 732 guideline [52] for environmental wind flow studies was used as the basis for computational domain size and model location. According to the guidelines, for a single structure with the height  $H$ , the horizontal distance separating the sidewalls of the structure and side boundaries of the computational domain must be  $5H$ . Similarly, the vertical distance separating the roof and the top of domain must also be  $5H$ . Along the direction of the flow, the distance between the inlet and the façade of the building must be  $5H$ . The distance between the leeward side and outlet, however, must be  $15H$  to allow for flow re-development behind the wake region. This is also considering that for steady RANS calculations, fully developed flows are generally assumed as the boundary condition [52].

Fig. 25. Computational domain of building with aero-elastic belt devices

Due to the complex nature of the model, a non-uniform mesh was utilised for volume and surfaces of the computational domain [53]. The generated computational mesh of the building model is shown in Figure 26. The grid was improved and refined according to the relevant critical areas for the simulation e.g. the aero-elastic belt. The scales of the mesh element were stretched smoothly to resolve the areas with high gradient mesh and to enhance the precision of the results. The inflation factors were adjusted with respect to the intricacy of the geometry face elements. This was employed to generate a finely resolved mesh perpendicular to the wall and coarse mesh parallel to it [54].

Fig. 26. (a) Computational grid (b) Sensitivity analysis

Sensitivity analysis was performed in order to confirm the computational modelling of the building integrated with the aero-elastic belt. The computational grid was established on a sensitivity analysis which was conducted by performing supplementary simulations with the same domain and boundary conditions but with various grid sizes. This procedure then enlarged the number of elements from 2.44 M elements (coarse) to 4.90 M elements (fine). The mean value of the wind speed in the vertical line of the R1 belt was invoked as the error gauge (Figure 27 (b)). The maximum error among the fine mesh and medium mesh was 3.4% or  $\pm 0.08$  m/s while the mean error was 1%. Therefore, the redundancy of model simulation with finer mesh had no significant effects on the solutions.

The boundary conditions were specified according to the AIJ guidelines [55]. The airflow velocity profile and turbulent kinetic energy (TKE) were enforced on the inlet region which were based on [50], with the stream-wise velocity of the incident airflow conforming to the power law with an alpha equal to 0.25. This exponent corresponds to a sub-urban terrain (See Figure 27). The  $\epsilon$  values for the  $k$ - $\epsilon$  turbulence model

were obtained through the assumption of a local equilibrium of  $P_k = \varepsilon$  [50]. Standard wall functions [56] were invoked for wall boundaries excluding the ground. The ground region had adjusted wall functions relying on roughness values [57]. Based on literature [57], this has to stipulated by an equivalent sand-grain roughness height  $k_s$  and roughness constant  $C_s$ . The non-homogeneous of the ABL in the horizontal dimension was limited by a suitable sand-grain roughness height and roughness constant adapted for the inlet profiles, obeying the equation of [58] :

$$k_s = \frac{9.793z_0}{C_s} \quad (12)$$

where  $z_0$  is the aerodynamic roughness height for sub-urban topography. Sand-grain roughness height was set to 1.0 mm and roughness constant was set to 1.0 [51]. The side walls and top wall of the domain were fixed as symmetry. This indicated zero velocity in the normal direction and zero gradients for all pertinent variables at the side and top walls. Zero static pressure was utilised for the outlet boundary. The boundary conditions are reviewed in Table 1.

Fig. 27. (a) Velocity profile (b) TKE profile of approach wind flow [51]

Table 1. Summary of boundary conditions for the CFD model

The solution convergence and pertinent variables were observed and the solution was considered to be complete upon observation of invariant iterations. Furthermore, property conservation was also tested if attained for the converged solution, which was executed by running a mass flux balance. This selection was obtainable from the FLUENT flux report panel which permits the calculation of mass flow rate for boundary zones. For the current model, the mass flow rate balance was lower than the required value equivalent to a value less than 1% of minimum flux through domain boundaries, i.e. inlet and outlet.

### 3.2 Estimation of wind power

The study utilised regression analysis using a polynomial curve of degree three to extrapolate power output given integral-value wind speed. Experimental data from [6] was used, with varying wind speed and the corresponding output power, using the optimal load and tension for an aero-elastic belt. A degree three polynomial is analogous to the fundamental equation for wind power making the choice for this polynomial type more sensible. Regression analysis was able to obtain an R-squared value of 0.9666. Using the manufacturer's specifications, cut-in wind speed is limited to 3 m/s. Therefore in order to extract results using the same aero-elastic belt, reconfiguration of the belt has to be done on installations on areas of the buildings with wind speeds lower than 3 m/s. This investigation simulated a gentle breeze, which is category 3 in the Beaufort wind force scale.

### 3.3 Method validation

Figure 28 (a) and (b) show a comparison between the experimental PIV results of [51] and the current modelling values for the airflow speed distribution around the building model. The values for the airflow speed close to the windward wall seem to be at a lower speed in the model compared to the PIV results, however a similar pattern was observed for most areas particularly close to the roof. Figure 28 (c) and

(d) show a comparison between the prediction of the current model and [51] of the pressure coefficient distribution around the building model.

Fig. 28. (a) PIV measurements of velocity [51] (b) velocity distribution in the current model (c) pressure coefficient result [51] (d) pressure coefficient distribution in the current model.

#### 4. RESULTS AND DISCUSSION

Figure 29 displays the contours of the velocity field for the side view cross-sectional area within the computational domain denoting the airflow distribution around the building integrated with aero-elastic belt. On the left part of the plot the scale of airflow speed is displayed in m/s. Colour coding was employed to better illustrate the fluid domain contour plots which range from 0 to 5.9 m/s. As observed, the incident wind flowed from the right side of the domain and subsequently the airflow decreased in speed as it moved towards the building and was then lifted upwards. Regions of flow separation were detected on the lower windward side of the structure and also at the leeward side of the building and roof. Zoomed in views of the velocity distribution around the aero-elastic belt R1, R2 and R3 are shown on top of the diagram. The results showed that the shape and angle of the roof had a significant influence to the performance of the aero-elastic belt. In the diagram, it is clear that locating the device at the leeward side of the roof will result in little to no energy generation due to the low wind speeds in this area. However, it should be noted that this was not the case for other wind angles, for example when the wind is from the opposite direction. Therefore, location surveying, wind assessment and detailed modelling are very important when installing devices in buildings. At wind velocity ( $U_H$ ) 4.7 m/s and  $0^\circ$  wind direction, the airflow speed in R1 was the highest at 4.5m/s while the lowest was observed for the R2 aero-elastic belt located at the centre of the roof.

Fig. 29. Contours of velocity magnitude showing a cross-sectional side view of the building

Figure 30 displays the top view cross-section area for the velocity contours within the computational domain indicating the airflow distribution around the building integrated with aero-elastic belt. The incident wind flowed from the right border of the domain and the airflow decreased in speed as it flowed closer to the building and accelerated as it flowed around the corners. Regions of flow separation were detected on the leeward and side areas of the building. Zoomed in views of the velocity distribution around the aero-elastic belt F1-F3 and S1-S3 are shown on top and right side of the diagram. At wind velocity ( $U_H$ ) 4.7 m/s and  $0^\circ$  wind direction, the airflow speed in F1 and F3 were the highest at 5.4m/s while the lowest was observed for the S2 and F2 aero-elastic belts located at the airflow recirculation zones.

Fig. 30. Contours of velocity magnitude showing a cross-sectional top view of the building

Figure 31 compares the maximum air velocity speed measured at the belt location for roof installations R1, R2 and R3 at various wind directions. These setups behaved in a trend similar to each other, but the notable highest velocities were attained from the R3 or apex installation. These setups had peak velocity values occurring at the region between  $30^\circ$  to  $60^\circ$  orientation, with the maximum value obtained at  $30^\circ$ . There

was significant speed decrease after 60° that could be attributed to the belt frame corners which impeded the wind from flowing through the belt region and therefore would reduce its performance or not allow the belt to flutter

Fig. 31. Effect of wind direction on the wind speed at belt located on the roof for various wind angle of approach with outdoor wind  $U_H = 10$  m/s

Figures 32 and 33 compare the maximum air velocity speed measured at the belt location for the windward and side installations, respectively at various wind directions. When comparing the two figures it was observed that the plot of F3 had a similar trend with the S1 belt which showed a significant performance drop in terms of velocity between 20-60°. This was also due to the frame of the wind belt which impeded the wind from flowing through the belt region and therefore would reduce its performance or not allows the belt to flutter

While the plot of F1 was a mirrored of S3, and F2 was mirrored S2. There is some symmetry that can be expected as observing the locations in Figure 24. It is not a perfect symmetry due to the roof shape having some effect on airflow. Looking at the location with highest velocity values for the front side of the building, there was a significant decrease in velocity from 10° to 40°, accounting for approximately 83% speed reduction, and same increase in speed was observed from 40° to 70°. For the side installation S1 the tipping point was at 50° where the change in angle exposure past this point marked significant increase in velocity. From the results it was clear that both the location of the device and wind direction had a significant effect on the air speed achieved at the belt location. Therefore a complete detailed analysis of these factors should be carried out when integrating wind belts to buildings to ensure that the performance is optimised and also minimised the number of belts integrated to the building.

Fig. 32. Effect of wind direction on the wind speed at belt located on the windward side of building with outdoor wind at  $U_H = 10$  m/s

Fig. 33. Effect of wind direction on the wind speed at belt located on the side of building with outdoor wind at  $U_H = 10$  m/s

Figure 34 illustrates the effect of different outdoor wind speed  $U_H$  values of 2, 4, 6, 8, and 10 m/s at 0° wind direction on the air speed achieved at the belt location. Similar trend was observed for all the curves with the highest speed achieved in R1 and F3 and lowest speed achieved in F2 and S2. The increase in the velocity profile corresponded to a proportional increased for the wind speed for all the belt locations.

Fig. 34. Wind speeds gathered at belt position for various mounting locations for 0° wind angle of approach

Figure 35 depicts velocity results for 90° wind angle approach. At this angle the output of the roof installations were overtaken by those in the front and side, most notably by F3, S1 and S3 mainly because of the geometry of the belt frame. The frame restricts airflow in the perpendicular direction to the belt. Therefore for locations with this type of prevailing wind direction it will be better for the aero-elastic belts to be integrated through the front and side edges of the building.

Fig. 35. Wind speeds gathered at belt position for various mounting locations for 90° wind angle of approach

Figure 36 compares the estimated output of the device at various locations and wind directions of 0 to 90°, in increments of 10 degrees while maintaining a uniform outdoor wind velocity ( $U_H = 10$  m/s). F1, F2 and F3 represent the aero-elastic belt mounted on the front face of the building; S1, S2 and S3 represent those on the side face, while R1, R2 and R3 are those for the roof locations. As observed, the highest power output comes from location R3 – the apex of the building – with an estimated output of 200.54 mW, resulting from wind speed that accelerated up to approximately 14.4 m/s, approximately 37.5% speed-up at the particular height. This occurred for an incoming wind 30° relative to the building facade.

Depending on prevailing wind direction of the area, the installation location of the belt can be determined. The green trendline represents the power output trend for R3, the location with the highest total power generation summed over 0 to 90 degrees. The brown trendline shows the trend for S2, the location with the lowest summed power generation over the same angular range.

Secondary to the building apex, locations on the edge also provide well above-average power output. Based on the simulated conditions, locations S3, F1 and R1 should be optimum locations for building integration of the aero-elastic belt, considering the power averages for 0, 45 and 90-degree orientations.

The last locations an installer would want to put an aero-elastic belt on are the central areas of the building's faces (illustrated by F2 and S2). Taking into account angular averages these locations provided the least amount of power, with no power generated at all for some cases due to the wind speed not being able to make it to the aero-elastic belt's cut-in wind speed for generation. This finding can be considered by some to be a counterintuitive result, considering these locations are directly hit by the oncoming wind.

Fig. 36. Sample calculation based on aero-elastic belt (2-magnet-coil system) data measured from experimental data [6]

Figure 37 compares the estimated output of the device located in the three locations F3, S3 and R3 at various outdoor wind speeds. Among these three locations, at 30° wind direction, R3 provided the highest output ranging between 59 to 200 mW, while F3 showed the lowest output and only started to generate at outdoor wind velocity ( $U_H$ ) above 4 m/s.

Fig. 37. Impact of different outdoor wind speeds ( $U_H$ ) on the estimated output of the aero-elastic belt for locations F3, S3 and R3

## 5. CONCLUSIONS AND FUTURE WORKS

The aero-elastic belt is beneficial for low-energy wind harvesting in the built environment due to its low cost and modularity. The necessity of investigating the integration of the aero-elastic belt into buildings utilising CFD analysis is evident. The review of previous works on the aero-elastic belt showed that several authors have assessed the performance of the device in uniform flows in the laboratory or wind tunnel but did not investigate the effect of buildings on its performance. Therefore, the current work addressed the issue by carrying out CFD modelling of a simplified building model integrated with aero-elastic belts. The work investigated the effect of various wind speeds and aero elastic belt locations on the performance of the device. The simulation used a gable-roof type building model with a  $27^\circ$  pitch obtained from the literature. The ABL flow was utilised for the simulation of the incident wind. The three-dimensional Reynolds-averaged Navier-Stokes equations jointly with the momentum and continuity equations were solved through ANSYS FLUENT 16 for obtaining the flow velocity field and pressure field. Sensitivity analyses for the CFD grid resolutions were implemented for verification of modelling. The results of the flow around the buildings and pressure coefficients were validated with previous experimental work. The study utilised regression analysis and experimental data to estimate the power output of the aero-elastic belt.

In terms of potential for power generation from the aero-elastic belt, the apex of the roof or the highest point of the building recorded the highest power yield, with this location's production being the largest with the 45-degree approach of the wind relative to the building. Optimum placement of the aero-elastic belt would mean prioritising the roof and the trailing edges of the building, and not the leading edge nor centres of surfaces, to yield the highest possible power generation, depending on wind conditions.

Subject to the prevailing wind direction within the building environment, the installation location with the highest potential for energy output on the front and side faces of the building can be inferred with more confidence using the results of the study. With respect to the physical geometry of the frame of containing the belt, the cover can be further minimised to enable more wind to flow across the belt.

There is a potential for further scaling up the system in terms of size and configuration, with the plausibility of constructing an array of aero-elastic belts. The results showed the importance of using detailed CFD analysis to evaluate the aero elastic belt. The detailed velocity distribution results showed the capabilities of CFD on assessing the optimum location of the devices around the building. The modelling procedure and data presented in this work can be used by engineers/researchers to further investigate the integration of the aero-elastic belt in the urban environment.

Future studies on the aero-elastic belt installation in buildings will include simulations using transient models which take into account non-uniform flow conditions. Prospective investigations on the impact of varying shapes of the subject building

and also different locations of the device will also be conducted. Further studies will investigate the impact of surrounding buildings on the performance of the device as well. This will incorporate the shape of surrounding buildings, distance and positioning, etc. Field tests will also be carried out to evaluate device performance in actual conditions and assess other factors such as noise, visual and related parameters. Economic analysis of the integration of the aero-elastic belt in buildings will be conducted and compared with more established low-energy generation devices.

## NOMENCLATURE

### Symbols

$U$	Air velocity (m/s)
$p$	Static pressure (Pa)
$H$	Height (m)
$L$	Length (m)
$W$	Width (m)
$x, y, z$	Direction
$g$	gravitational acceleration (m/s <sup>2</sup> )
$S_M$	Mass added to the continuous phase from the dispersed second phase
$\tau$	Time in the past contributing in the integral response
$k_{eff}$	Effective conductivity (W/mk)
$\vec{J}_j$	Diffusion flux
$S_h$	Heat of chemical reaction and other volumetric heat source defined by user
$k$	Turbulence kinetic energy (m <sup>2</sup> /s <sup>2</sup> )
$\epsilon$	Turbulence dissipation rate (m <sup>2</sup> /s <sup>3</sup> )
$G_k$	Generation of turbulent kinetic energy due to the mean velocity gradients
$G_b$	Generation of turbulence kinetic energy due to buoyancy
$Y_M$	Fluctuating dilatation in compressible turbulence to the overall dissipation rate
$\sigma_k$	Turbulent Prandtl numbers for turbulence kinetic energy
$\sigma_\epsilon$	Turbulent Prandtl numbers for energy dissipation rate
$S_k$	User defined source term for turbulence kinetic energy
$S_\epsilon$	User defined source term for energy dissipation rate
$k_s$	sand-grain roughness height (m)
$c_s$	roughness constant
$z_0$	Aerodynamic roughness length (m)
F1, F2, F3	Front aero-elastic belts
S1, S2, S3	Side aero-elastic belts
R1, R2, R3	Roof aero-elastic belts
$P$	Power generated
$P_Y(t)$	Plunging contribution to the power
$P_\theta(t)$	Pitching contribution to the power
$F_Y(t)$	y-component of force
$V_Y(t)$	Plunging velocity
$U_\infty$	Free-stream velocity
$M(t)$	Torque about pitching centre

$\omega(t)$	Angular velocity
$C_P$	Instantaneous power coefficient
$C_{Pmean}$	Time-averaged power coefficient
$C_{Ph}$	Pitching contribution to the power coefficient
$C_{P\theta}$	Plunging contribution to the power coefficient
$T$	Oscillation frequency
$C_Y(t)$	Instantaneous lift coefficient
$C_M(t)$	Momentum coefficient
$\eta$	Power-extraction efficiency
$\theta_0$	Pitching amplitude
$A$	Overall vertical extent of foil motion

## Acknowledgement

The authors would like to thank the British Council and Department of Science and Technology for the funding (DOST-Newton Fund no.209559487) of this research.

## References

- [1] L. Pérez-Lombard, P.-L. Luis, O. José, and P. Christine, "A review on buildings energy consumption information," *Energy Build.*, vol. 40, no. 3, pp. 394–398, 2008.
- [2] F. Toja-Silva, T.-S. Francisco, P. Carlos, L.-G. Oscar, N. Jorge, and C. Ignacio, "On Roof Geometry for Urban Wind Energy Exploitation in High-Rise Buildings," *Computation*, vol. 3, no. 2, pp. 299–325, 2015.
- [3] Y. Hu *et al.*, "Self-Powered System with Wireless Data Transmission," *Nano Lett.*, vol. 11, no. 6, pp. 2572–2577, 2011.
- [4] G. Zhu, Z. Guang, Y. Rusen, W. Sihong, and Z. L. Wang, "Flexible High-Output Nanogenerator Based on Lateral ZnO Nanowire Array," *Nano Lett.*, vol. 10, no. 8, pp. 3151–3155, 2010.
- [5] Y. Hu, H. Youfan, Z. Yan, X. Chen, Z. Guang, and Z. L. Wang, "High-Output Nanogenerator by Rational Unipolar Assembly of Conical Nanowires and Its Application for Driving a Small Liquid Crystal Display," *Nano Lett.*, vol. 10, no. 12, pp. 5025–5031, 2010.
- [6] D. Pimentel, P. Musilek, A. Knight, and J. Heckenbergerova, "Characterization of a wind flutter generator," in *2010 9th International Conference on Environment and Electrical Engineering*, 2010.
- [7] F. Fei, Z. Shengli, M. John, and L. Wen, "Development of an Indoor Airflow Energy Harvesting System for Building Environment Monitoring," *Energies*, vol. 7, no. 5, pp. 2985–3003, 2014.
- [8] Y. K. Tan, Z. Dabin, and B. Steve, "Wind Energy Harvesting for Recharging Wireless Sensor Nodes: Brief Review and A Case Study," in *Introducing Energy Harvesting to Sensor Networks*, 2014, pp. 1–30.
- [9] "Application of Sensors in Cities," *50 Sensor Applications for a Smarter World - Libelium*. [Online]. Available: <http://www.libelium.com>. [Accessed: 27-Jul-2016].
- [10] Y. de C. Antoine Bonnabel, "Emerging Energy Harvesting Devices," Yole Développement, Oct. 2012.
- [11] G. Arioli, A. Gianni, and G. Filippo, "A new mathematical explanation of what triggered the catastrophic torsional mode of the Tacoma Narrows Bridge," *Appl. Math. Model.*, vol. 39, no. 2, pp. 901–912, 2015.
- [12] Y. Xie, X. Yonghui, L. Kun, and Z. Di, "Investigation on energy extraction performance of an oscillating foil with modified flapping motion," *Renewable Energy*, vol. 63, pp. 550–557, 2014.

- [13] E. Arroyo, A. Emmanuelle, F. Shaohui, M. Luc, and K. L. Wood, "Experimental Study of an Omni-Directional Wind Fluttering Energy Harvester," in *Volume 3: Industrial Applications; Modeling for Oil and Gas, Control and Validation*, y, 2014.
- [14] D. Pimentel, P. Musilek, A. Knight, and J. Heckenbergerova, "Characterization of a wind flutter generator," in *2010 9th International Conference on Environment and Electrical Engineering*, 2010.
- [15] V. Dinh Quy, V. D. Quy, N. Van Sy, D. T. Hung, and V. Q. Huy, "Wind tunnel and initial field tests of a micro generator powered by fluid-induced flutter," *Energy for Sustainable Development*, vol. 33, pp. 75–83, 2016.
- [16] F. Fei, J. D. Mai, and W. J. Li, "A wind-flutter energy converter for powering wireless sensors," *Sens. Actuators A Phys.*, vol. 173, no. 1, pp. 163–171, 2012.
- [17] Dibin Zhu, Z. Dibin, B. Steve, T. John, W. Neil, and H. Nick, "A novel miniature wind generator for wireless sensing applications," in *2010 IEEE Sensors*, 2010.
- [18] X. Wang, W. Xiao, C. L. Pan, Y. B. Liu, and Z. H. Feng, "Electromagnetic resonant cavity wind energy harvester with optimized reed design and effective magnetic loop," *Sens. Actuators A Phys.*, vol. 205, pp. 63–71, 2014.
- [19] S.-H. Kim *et al.*, "An electromagnetic energy scavenger from direct airflow," *J. Micromech. Microeng.*, vol. 19, no. 9, p. 094010, 2009.
- [20] A. Munaz, M. Ahmed, and C. Gwi-Sang, "An electromagnetic energy harvester based on multiple magnet scavenging power from low frequency vibration," *Microsyst. Technol.*, 2015.
- [21] D.-A. Wang, W. Dung-An, C. Chun-Yuan, and P. Huy-Tuan, "Electromagnetic energy harvesting from vibrations induced by Kármán vortex street," *Mechatronics*, vol. 22, no. 6, pp. 746–756, 2012.
- [22] M. Demori, D. Marco, F. Marco, F. Vittorio, F. Stefano, and P. Pietro, "Energy Harvesting from Von Karman Vortices in Airflow for Autonomous Sensors," *Procedia Engineering*, vol. 87, pp. 775–778, 2014.
- [23] X. Shan, S. Xiaobiao, S. Rujun, L. Bo, and X. Tao, "Novel energy harvesting: A macro fiber composite piezoelectric energy harvester in the water vortex," *Ceram. Int.*, vol. 41, pp. S763–S767, 2015.
- [24] L. A. Weinstein, M. R. Cacan, P. M. So, and P. K. Wright, "Vortex shedding induced energy harvesting from piezoelectric materials in heating, ventilation and air conditioning flows," *Smart Mater. Struct.*, vol. 21, no. 4, p. 045003, 2012.
- [25] S. Li, L. Shuguang, Y. Jianping, and L. Hod, "Ambient wind energy harvesting using cross-flow fluttering," *J. Appl. Phys.*, vol. 109, no. 2, p. 026104, 2011.
- [26] D. St. Clair, A. Bibo, V. R. Sennakesavababu, M. F. Daqaq, and G. Li, "A scalable concept for micropower generation using flow-induced self-excited oscillations," *Appl. Phys. Lett.*, vol. 96, no. 14, p. 144103, 2010.
- [27] A. Erturk, W. G. R. Vieira, C. De Marqui, and D. J. Inman, "On the energy harvesting potential of piezoaeroelastic systems," *Appl. Phys. Lett.*, vol. 96, no. 18, p. 184103, 2010.
- [28] R. Dickson, "New Concepts in Renewable Energy," *Lulu Enterprises Inc*, 2008.
- [29] M. Bryant, R. L. Mahtani, and E. Garcia, "Wake synergies enhance performance in aeroelastic vibration energy harvesting," *J. Intell. Mater. Syst. Struct.*, vol. 23, no. 10, pp. 1131–1141, 2012.
- [30] J. M. McCarthy, A. Deivasigamani, S. Watkins, S. J. John, F. Coman, and P. Petersen, "On the visualisation of flow structures downstream of fluttering piezoelectric energy harvesters in a tandem configuration," *Exp. Therm. Fluid Sci.*, vol. 57, pp. 407–419, 2014.
- [31] T. Burton, N. Jenkins, D. Sharpe, and E. Bossanyi, *Wind Energy Handbook*. John Wiley & Sons, 2011.
- [32] J. McCarthy, S. Watkins, A. Deivasigamani, S. John, F. Coman, "An investigation of fluttering piezoelectric energy harvesters in off-axis and turbulent flows," *J. Wind Eng. Ind. Aerodyn.*, vol. 136, pp. 101–113, 2015.

- [33] S. Li, L. Shuguang, and L. Hod, "Vertical-Stalk Flapping-Leaf Generator for Wind Energy Harvesting," in *Volume 2: Multifunctional Materials; Enabling Technologies and Integrated System Design; Structural Health Monitoring/NDE; Bio-Inspired Smart Materials and Structures*, 2009.
- [34] M. J. S. S. Alben, "Flapping states of a flag in an inviscid fluid: bistability and the transition to chaos," *Phys. Rev. Lett.*, vol. 100, no. 7, pp. 074301–1–4, 2008.
- [35] W. B. Hobbs and D. L. Hu, "Tree-inspired piezoelectric energy harvesting," *J. Fluids Struct.*, vol. 28, pp. 103–114, 2012.
- [36] J. D. Hobeck and D. J. Inman, "Energy Harvesting From Turbulence-Induced Vibration in Air Flow: Artificial Piezoelectric Grass Concept," in *ASME 2011 Conference on Smart Materials, Adaptive Structures and Intelligent Systems, Volume 2*, 2011.
- [37] H. D. Akaydin, N. Elvin, and Y. Andreopoulos, "Wake of a cylinder: a paradigm for energy harvesting with piezoelectric materials," *Exp. Fluids*, vol. 49, no. 1, pp. 291–304, 2010.
- [38] X. Fu, H. Yang, "Study of hydrodynamic vibrations in dual bluff body vortex flowmeter," *Chin. J. Chem. Eng.*, vol. 9, pp. 123–128, 2001.
- [39] J. Peng, P. Jiegang, F. Xin, and C. Ying, "Flow measurement by a new type vortex flowmeter of dual triangulate bluff body," *Sens. Actuators A Phys.*, vol. 115, no. 1, pp. 53–59, 2004.
- [40] A. Venugopal, A. Amit, and S. V. Prabhu, "Influence of blockage and upstream disturbances on the performance of a vortex flowmeter with a trapezoidal bluff body," *Measurement*, vol. 43, no. 4, pp. 603–616, 2010.
- [41] J. Allen and A. Smits, "ENERGY HARVESTING EEL," *J. Fluids Struct.*, vol. 15, no. 3–4, pp. 629–640, 2001.
- [42] G. W. Taylor, J. R. Burns, S. A. Kammann, W. B. Powers, and T. R. Welsh, "The Energy Harvesting Eel: a small subsurface ocean/river power generator," *IEEE J. Oceanic Eng.*, vol. 26, no. 4, pp. 539–547, 2001.
- [43] L. Tang, T. Liaosha, M. P. Païdoussis, and J. Jin, "Cantilevered flexible plates in axial flow: Energy transfer and the concept of flutter-mill," *J. Sound Vib.*, vol. 326, no. 1–2, pp. 263–276, 2009.
- [44] R. Song, S. Rujun, S. Xiaobiao, L. Fengchi, L. Jinzhe, and X. Tao, "A Novel Piezoelectric Energy Harvester Using the Macro Fiber Composite Cantilever with a Bicylinder in Water," *NATO Adv. Sci. Inst. Ser. E Appl. Sci.*, vol. 5, no. 4, pp. 1942–1954, 2015.
- [45] S. P. Matova, R. Elfrink, R. J. M. Vullers, and R. van Schaijk, "Harvesting energy from airflow with a micromachined piezoelectric harvester inside a Helmholtz resonator," *J. Micromech. Microeng.*, vol. 21, no. 10, p. 104001, 2011.
- [46] Y. Xie *et al.*, "Rotary triboelectric nanogenerator based on a hybridized mechanism for harvesting wind energy," *ACS Nano*, vol. 7, no. 8, pp. 7119–7125, Aug. 2013.
- [47] Q. Liang, L. Qijie, Y. Xiaoqin, L. Xinqin, and Z. Yue, "Integrated multi-unit transparent triboelectric nanogenerator harvesting rain power for driving electronics," *Nano Energy*, vol. 25, pp. 18–25, 2016.
- [48] J. Bae *et al.*, "Flutter-driven triboelectrification for harvesting wind energy," *Nat. Commun.*, vol. 5, p. 4929, Sep. 2014.
- [49] S. Frayne, "Generator utilizing fluid-induced oscillations," 7573143 B2, 2009.
- [50] P. Sofotasiou, J. K. Calautit, B. R. Hughes, and D. O'Connor, "Towards an integrated computational method to determine internal spaces for optimum environmental conditions," *Comput. Fluids*, vol. 127, pp. 146–160, 2016.
- [51] Y. Tominaga, S.-I. Akabayashi, T. Kitahara, and Y. Arinami, "Air flow around isolated gable-roof buildings with different roof pitches: Wind tunnel experiments and CFD simulations," *Build. Environ.*, vol. 84, pp. 204–213, 2015.
- [52] J. Franke, A. Hellsten, K. Heinke Schlunzen, and B. Carissimo, "The COST 732 Best Practice Guideline for CFD simulation of flows in the urban environment: a summary," *Int. J. Environ. Pollut.*, vol. 44, no. 1/2/3/4, p. 419, 2011.

- [53] H. N. Chaudhry, J. K. Calautit, and B. R. Hughes, "Computational analysis of a wind tower assisted passive cooling technology for the built environment," *Journal of Building Engineering*, vol. 1, pp. 63–71, 2015.
- [54] J. K. Calautit and B. R. Hughes, "Wind tunnel and CFD study of the natural ventilation performance of a commercial multi-directional wind tower," *Build. Environ.*, vol. 80, pp. 71–83, 2014.
- [55] Y. Tominaga *et al.*, "AIJ guidelines for practical applications of CFD to pedestrian wind environment around buildings," *J. Wind Eng. Ind. Aerodyn.*, vol. 96, no. 10–11, pp. 1749–1761, 2008.
- [56] B. E. Launder and D. B. Spalding, "The numerical computation of turbulent flows," *Comput. Methods Appl. Mech. Eng.*, vol. 3, no. 2, pp. 269–289, 1974.
- [57] T. Cebeci and P. Bradshaw, "Conservation Equations for Mass, Momentum, and Energy," in *Physical and Computational Aspects of Convective Heat Transfer*, 1984, pp. 19–40.
- [58] B. Blocken, T. Stathopoulos, and J. Carmeliet, "CFD simulation of the atmospheric boundary layer: wall function problems," *Atmos. Environ.*, vol. 41, no. 2, pp. 238–252, 2007.

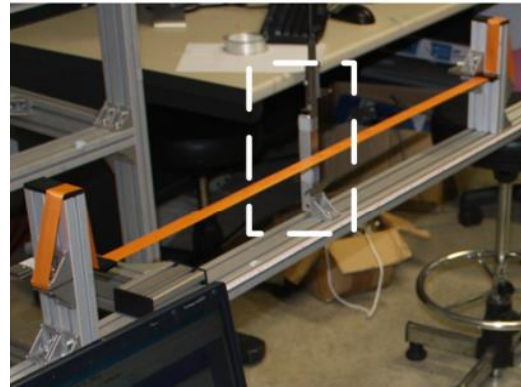
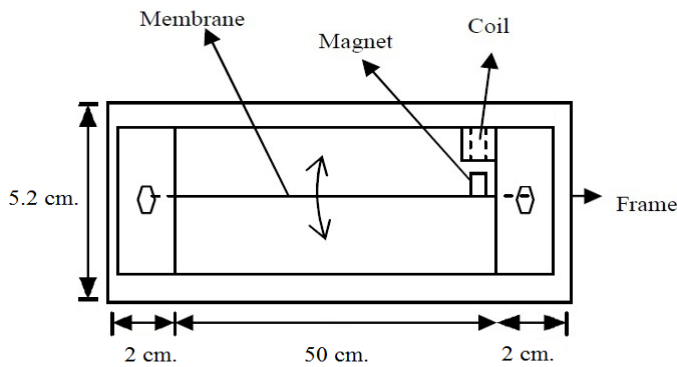


Fig 1. (a) Schematic diagram of an aero-elastic belt [6] (b) Example of experimental aero-elastic belt setup [7]

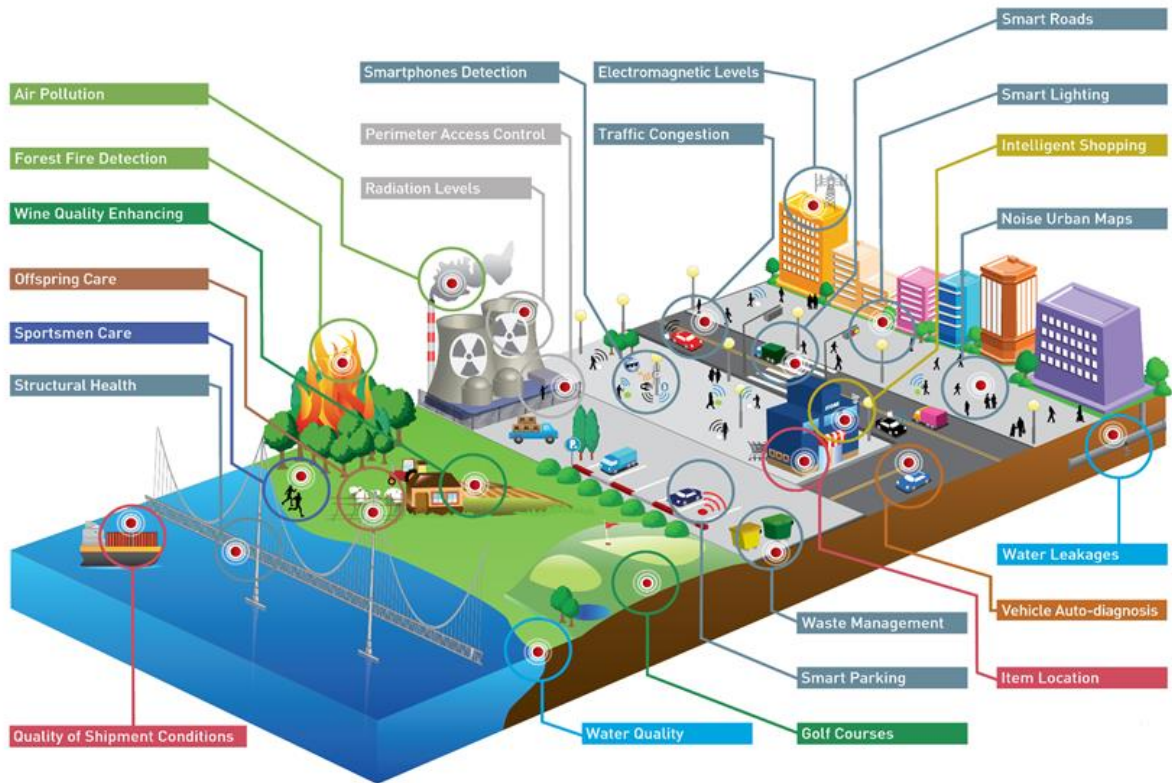


Fig. 2. Applications of wireless sensors in smart cities [9]

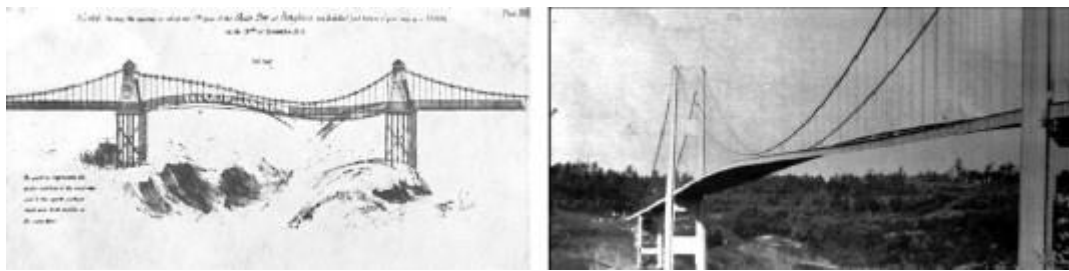


Fig. 3. (a) A painting of the Brighton Chain Pier collapse in 1836 (b) A photo of the Tacoma Narrows bridge collapse in 1941 [11]

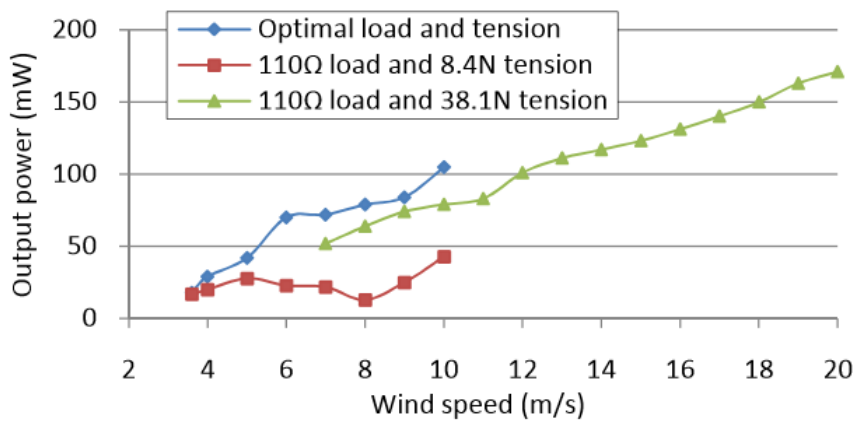


Fig. 4. Power output for the wind-belt experimental test setup in [14]

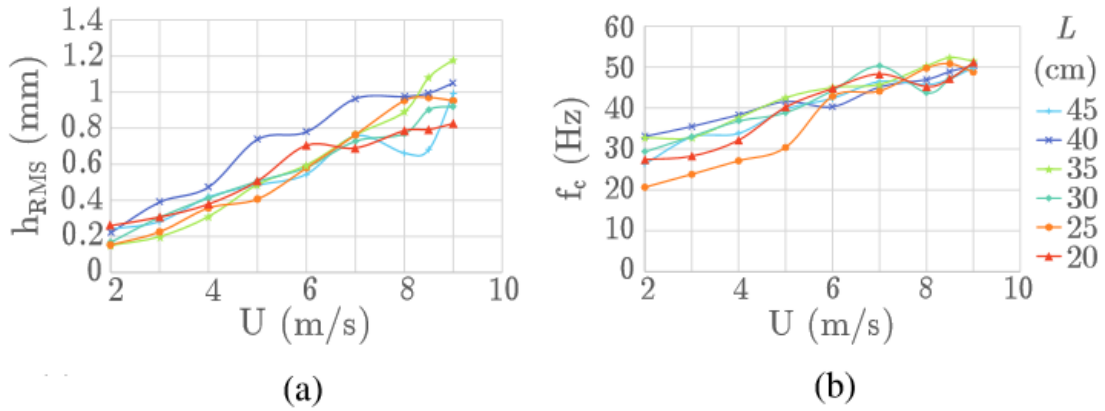


Fig. 5. (a) Amplitude and (b) Frequency of vibration as a function of wind speed for various ribbon lengths [13c]

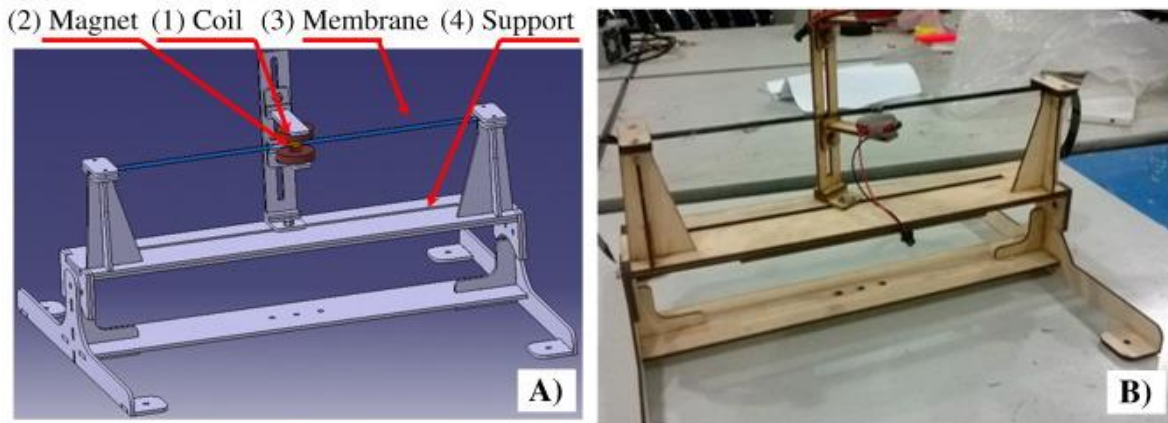


Fig. 6. (a) 3D model of the wind belt design and (b) Fabricated test model studied in [15]

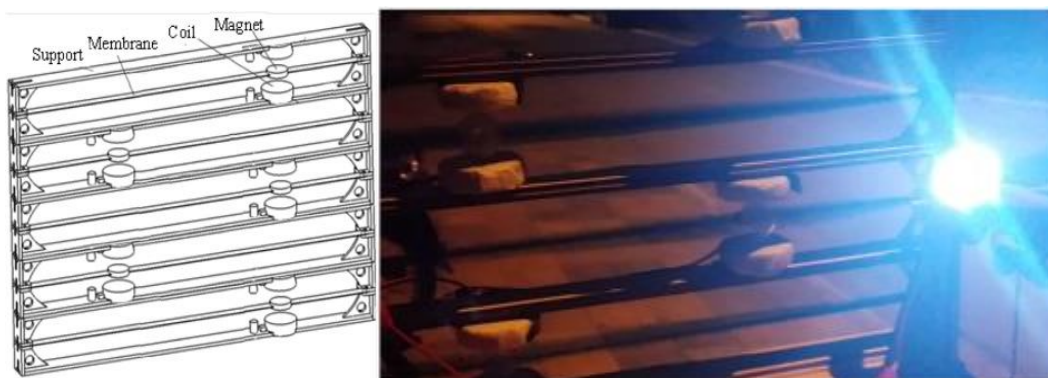


Fig. 7. (a) The 3D model of the windpanel - a combination of five windbelts (b) Testing of the windpanel powering an LED light in actual wind conditions [15]

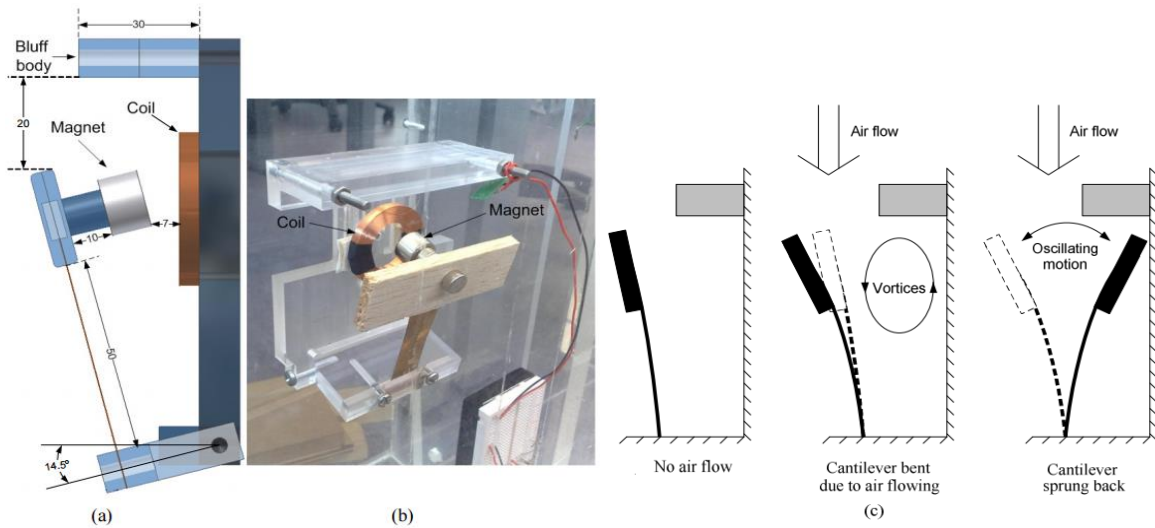


Fig. 8. (a) Schematic of energy harvester studied in [17] with measurements in mm (b) Experimental setup of the harvester (c) Operating principle of the energy harvester

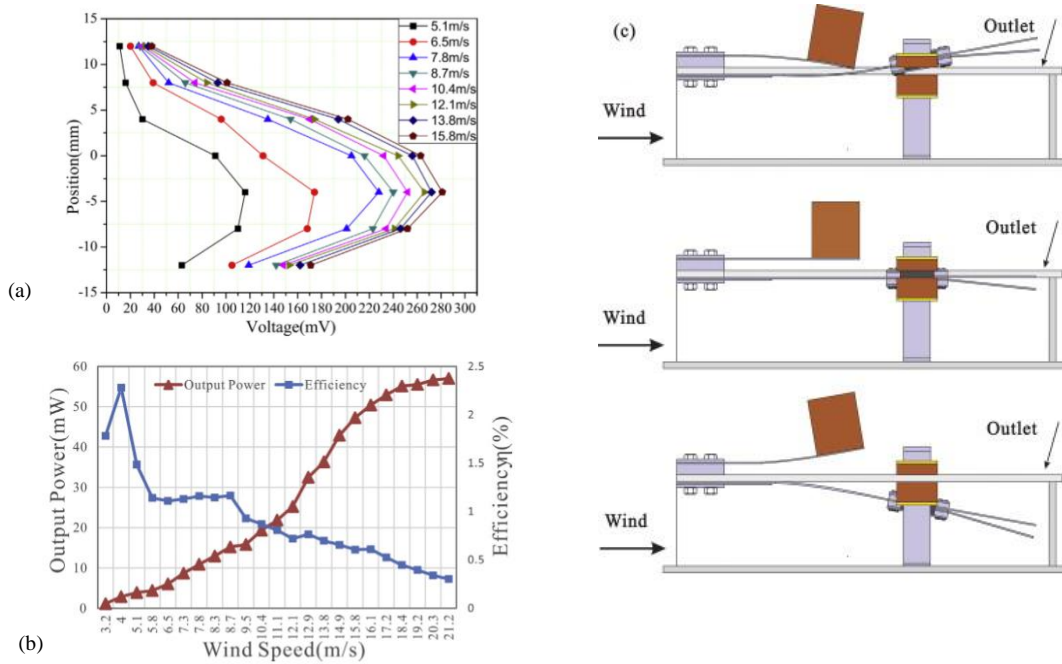


Fig. 9. (a) Output voltage vs. coil position [18] (b) Wind speed vs. max output power and efficiency (c) Working process of electromagnetic energy harvester [18]

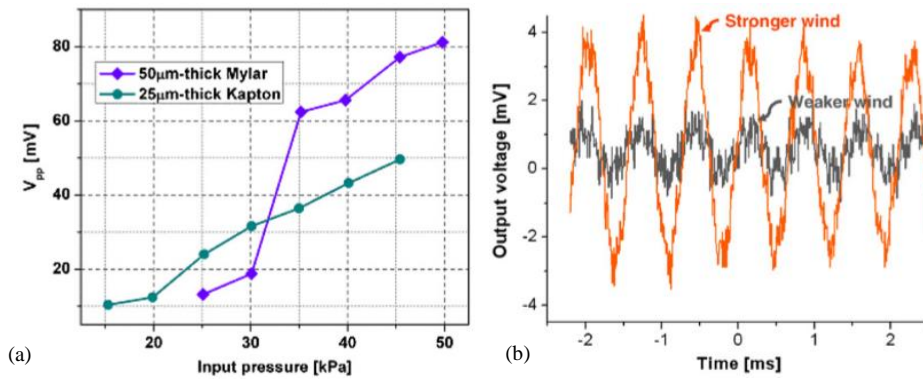


Fig. 10. (a) Measured peak-to-peak open-circuit voltage while varying input pressure (b) Output voltage in coil measured under weak and strong wind [19]

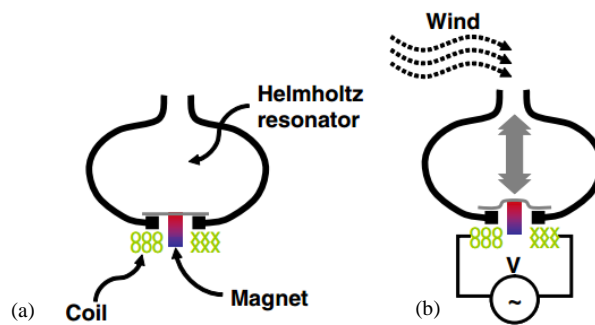


Fig. 11. Schematic plan illustrating the principle of operation of energy harvester in [19]: (a) at rest state; (b) at resonance through wind flow.

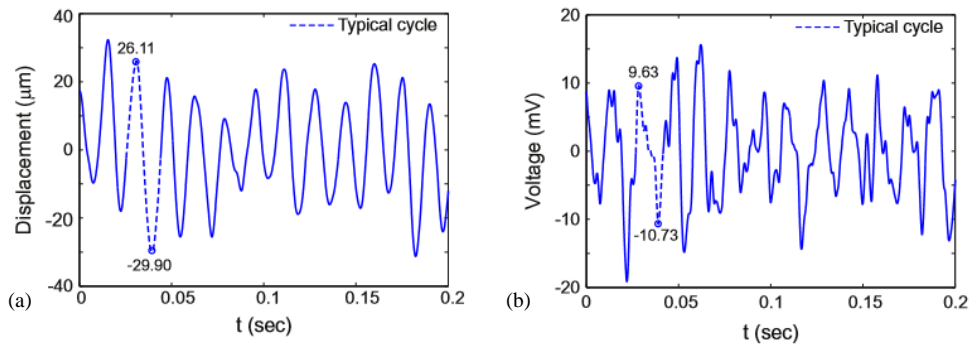


Fig. 12. (a) Magnet displacement and (b) Induced voltage by the coil for a typical cycle [21]

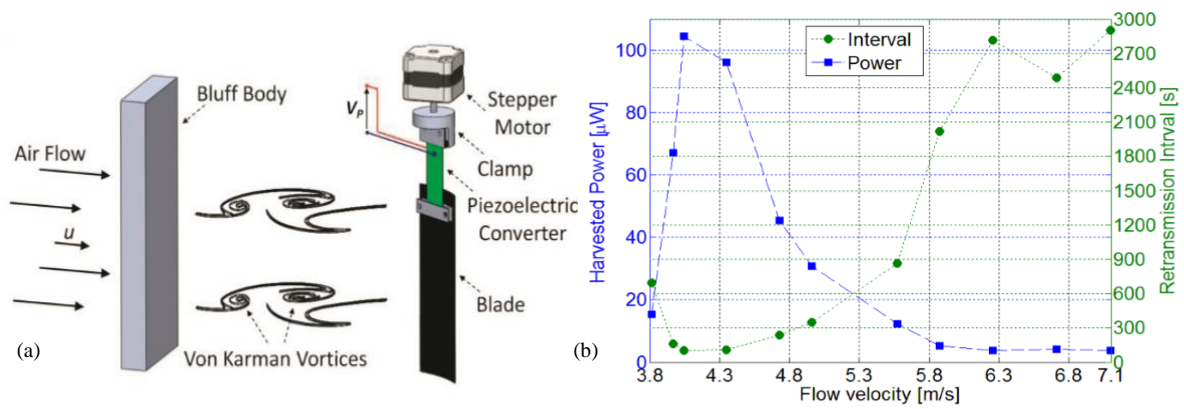


Fig. 13. (a) Schematic of the piezoelectric energy harvesting system (b) Average power output and retransmission time interval as a function of air flow velocity [22]

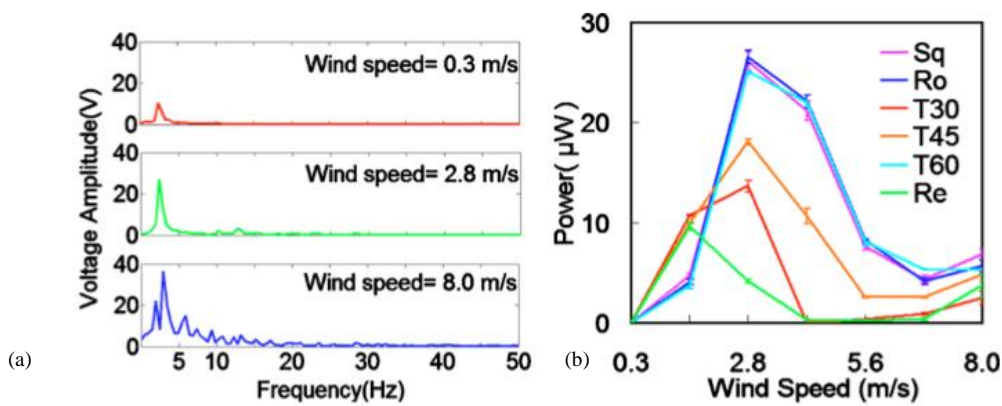


Fig. 14. (a) Wind response of piezo-leaf with varying wind speeds (b) Power output of the different shapes of piezo-leaf [25]

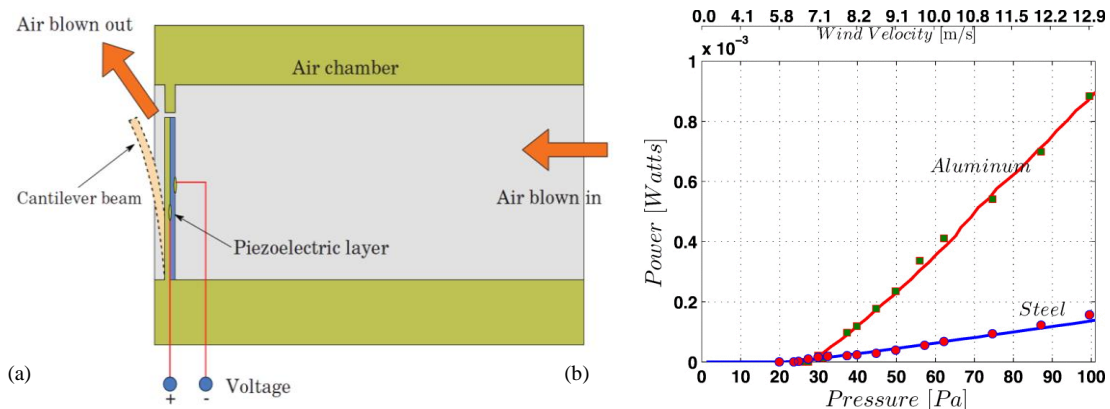


Fig. 15. (a) Piezoelectric energy harvester utilizing flow-induced oscillations (b) Maximum power output as function of air pressure for two beam types – Aluminium and Steel [26]

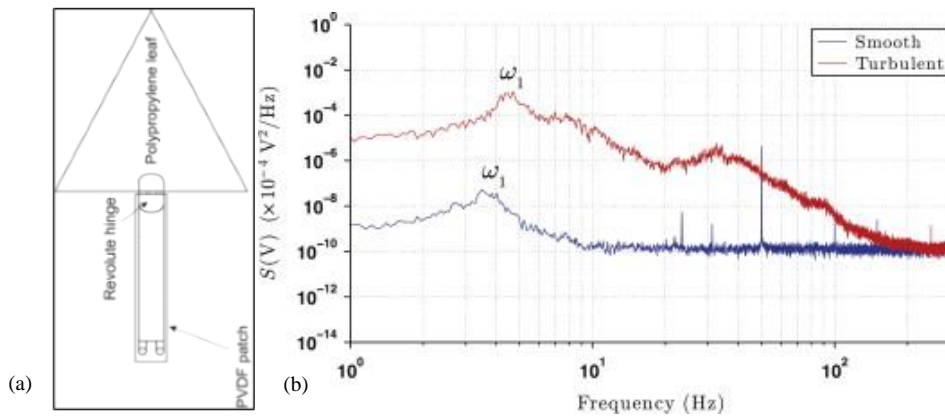


Fig. 16. (a) The Polyvinylidene-fluoride (PVDF) [28] leaf; and (b) Harvester's voltage spectral density for smooth and turbulent wind flow of 8 m/s at 135° flow angle [32]

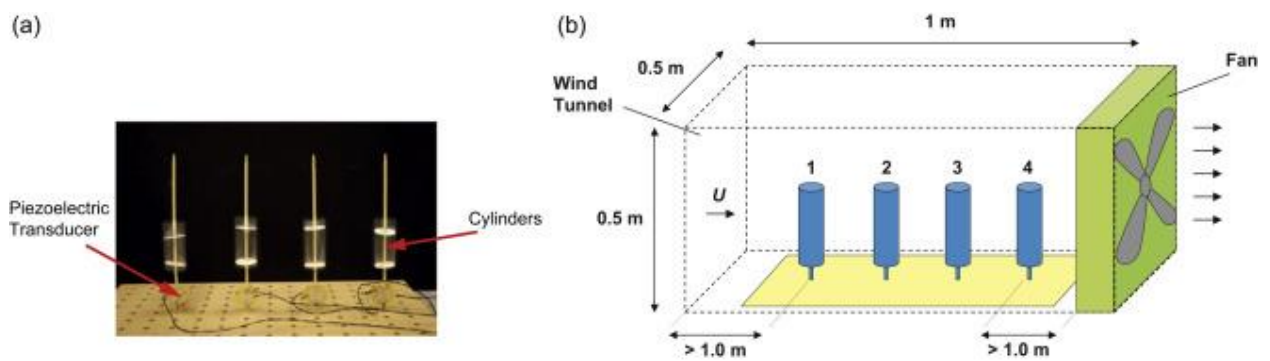


Fig. 17. (a) Experimental setup and (b) schematic diagram of parallel circular cylinders studied by [35]

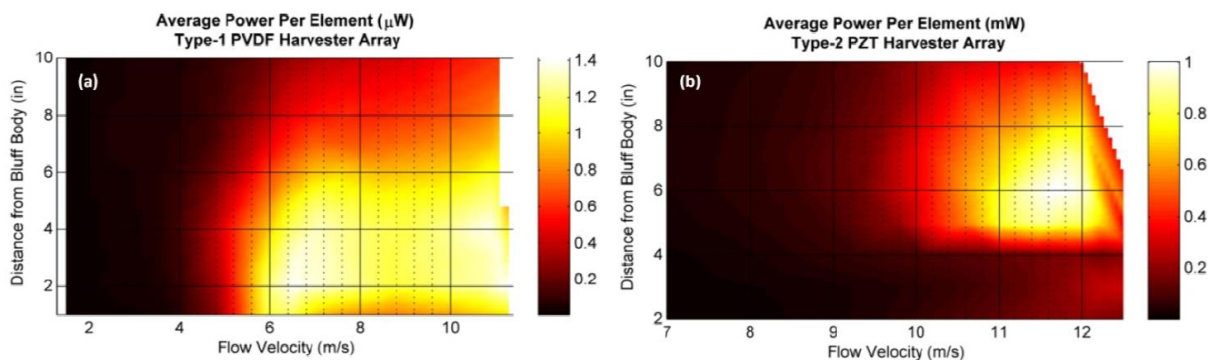


Fig. 18. Power output with varying flow velocity and bluff body position for (a) PVDF harvester array, and (b) PZT harvester array [36]

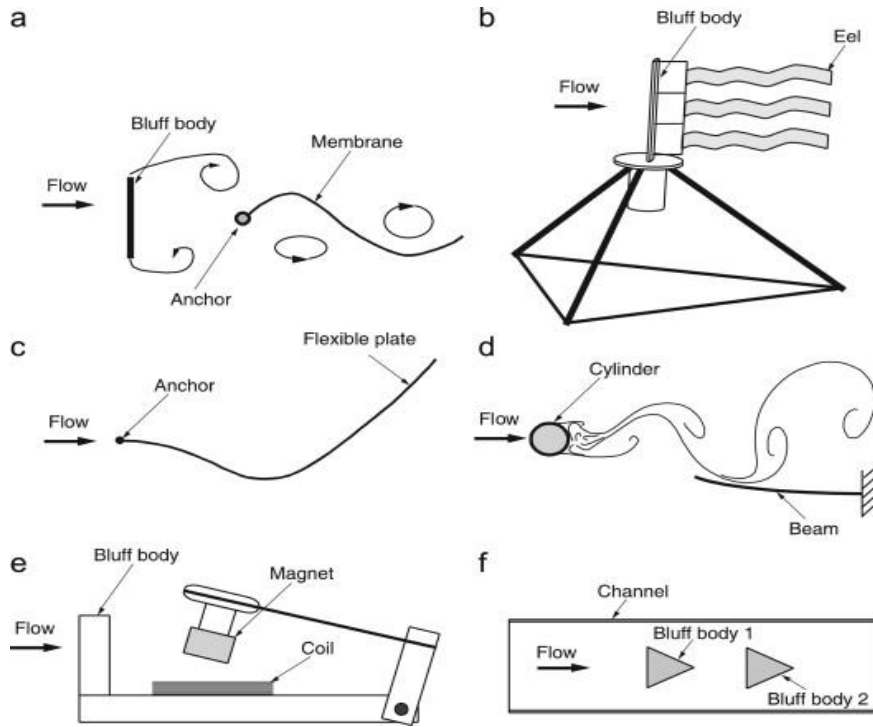


Fig. 19. Schematic diagrams showing different energy harvesting devices presented in (a) [41]; (b) [42]; (c) [43]; (d) [37]; (e) [17]; (f) [38]

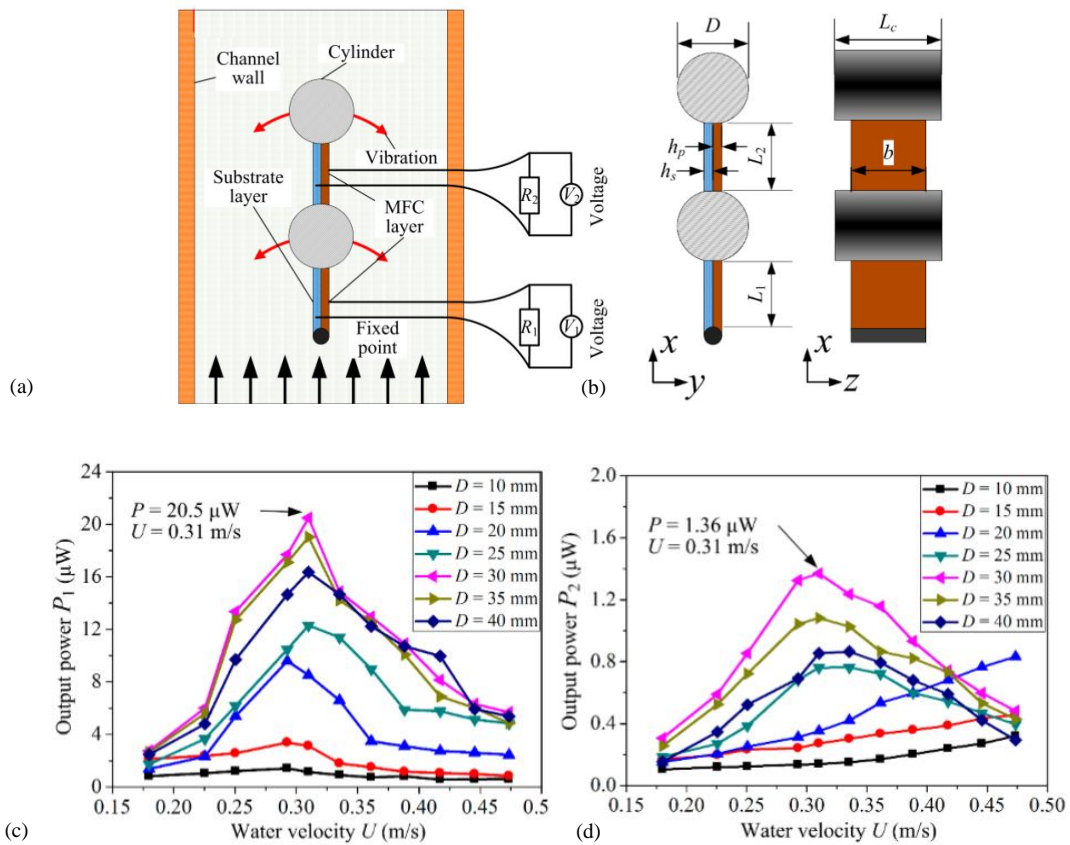


Fig. 20. (a) Schematic diagram; (b) x-y planar diagram; and generated power as function of water velocity with varying cylinder diameters for (c) upstream beam (d) downstream beam [44]

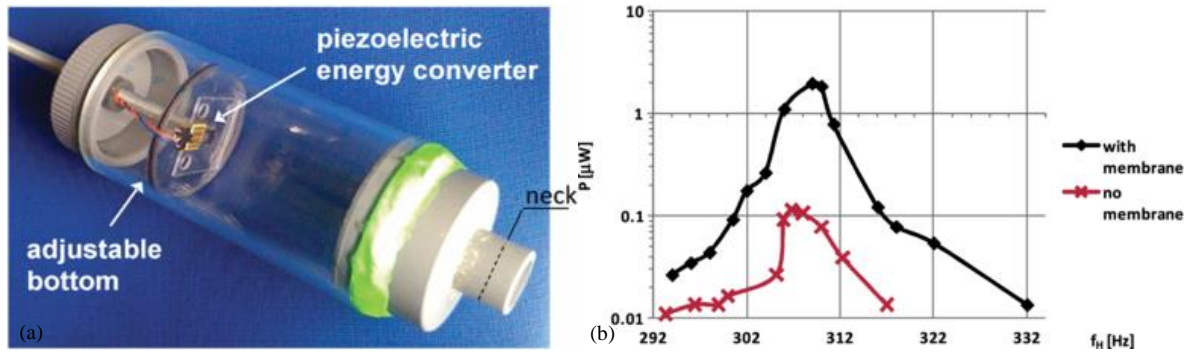


Fig. 21. (a) Helmholtz resonator with piezoelectric energy harvester (b) Power output of harvester for airflow of 14 m/s with resistance of 3.3 MΩ [45]

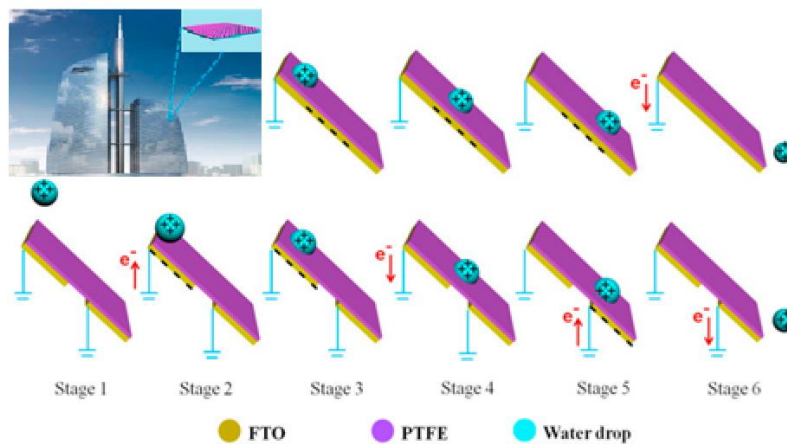


Fig. 22. Working mechanism leading to the improved efficiency of the MT-TENG; inset shows potential application in buildings [47]

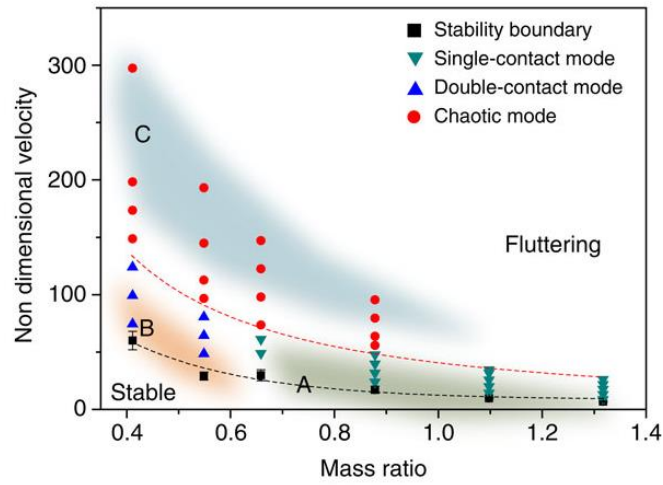


Fig. 23. Velocity vs. mass ratio plot of the relationship between flag and plate behaviour showing the different contact modes [48].

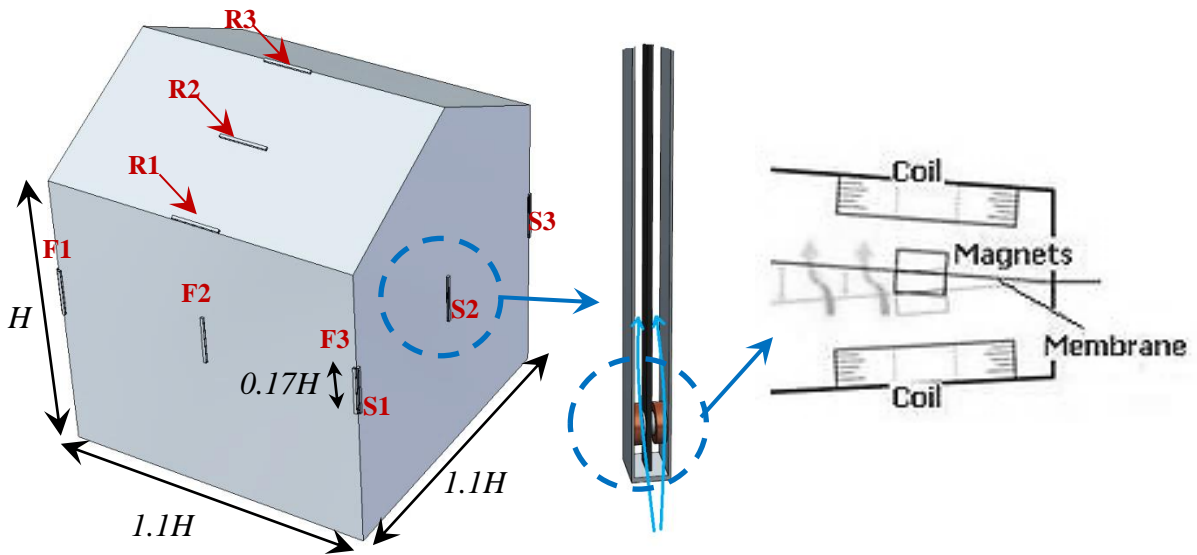


Fig. 24. CAD geometry of building with aero-elastic belt devices

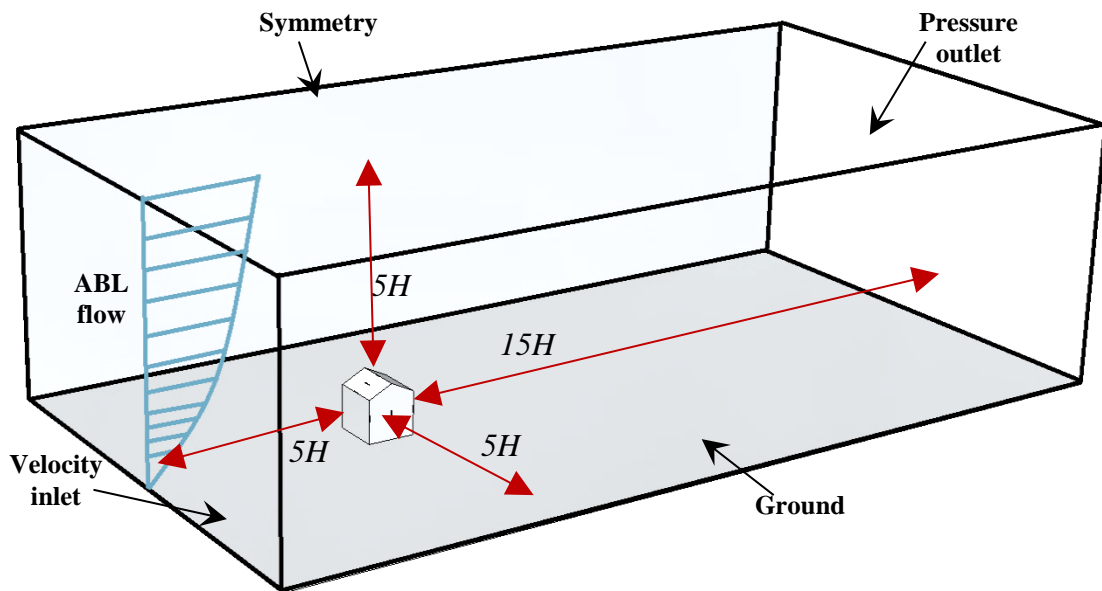


Fig. 25. Computational domain of building with aero-elastic belt devices

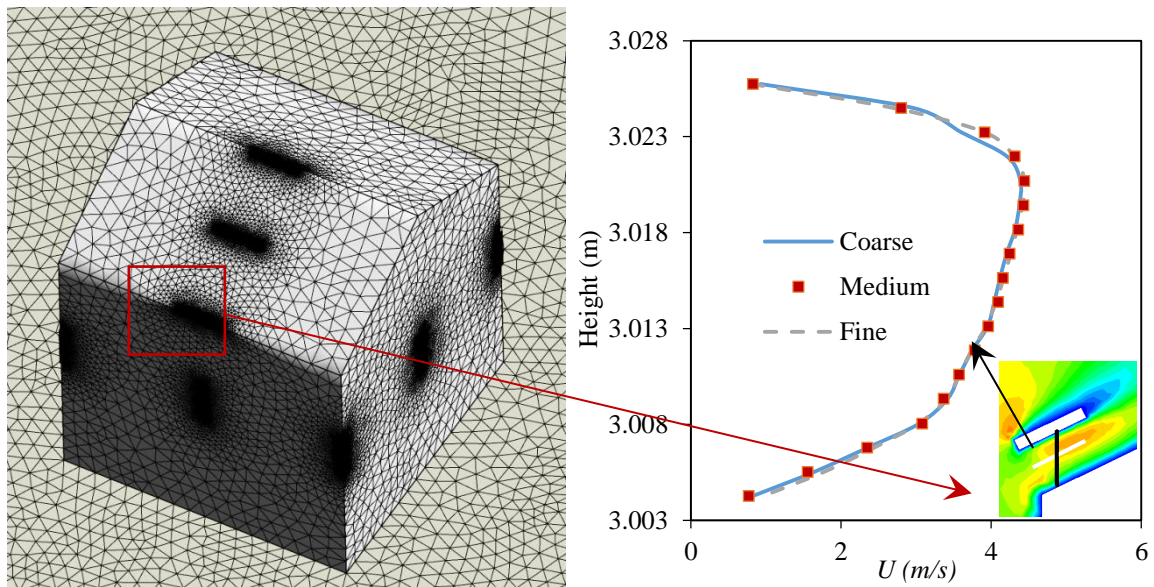


Fig. 26. (a) Computational grid (b) Sensitivity analysis

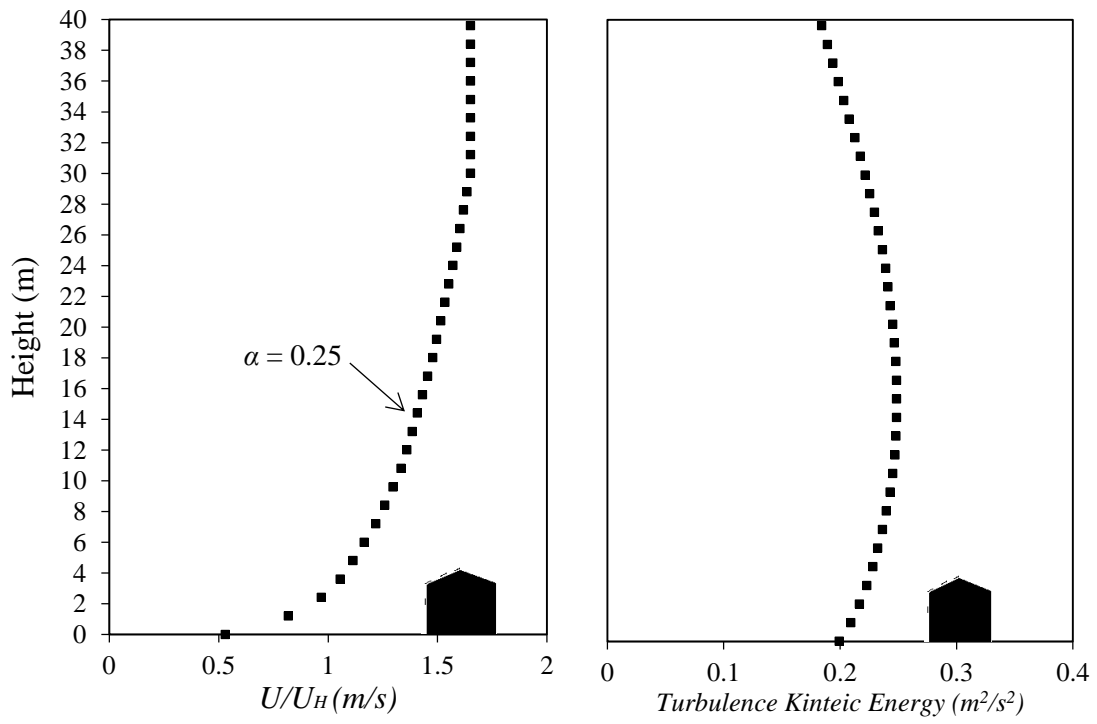


Fig. 27. (a) Velocity profile (b) TKE profile of approach wind flow [51]

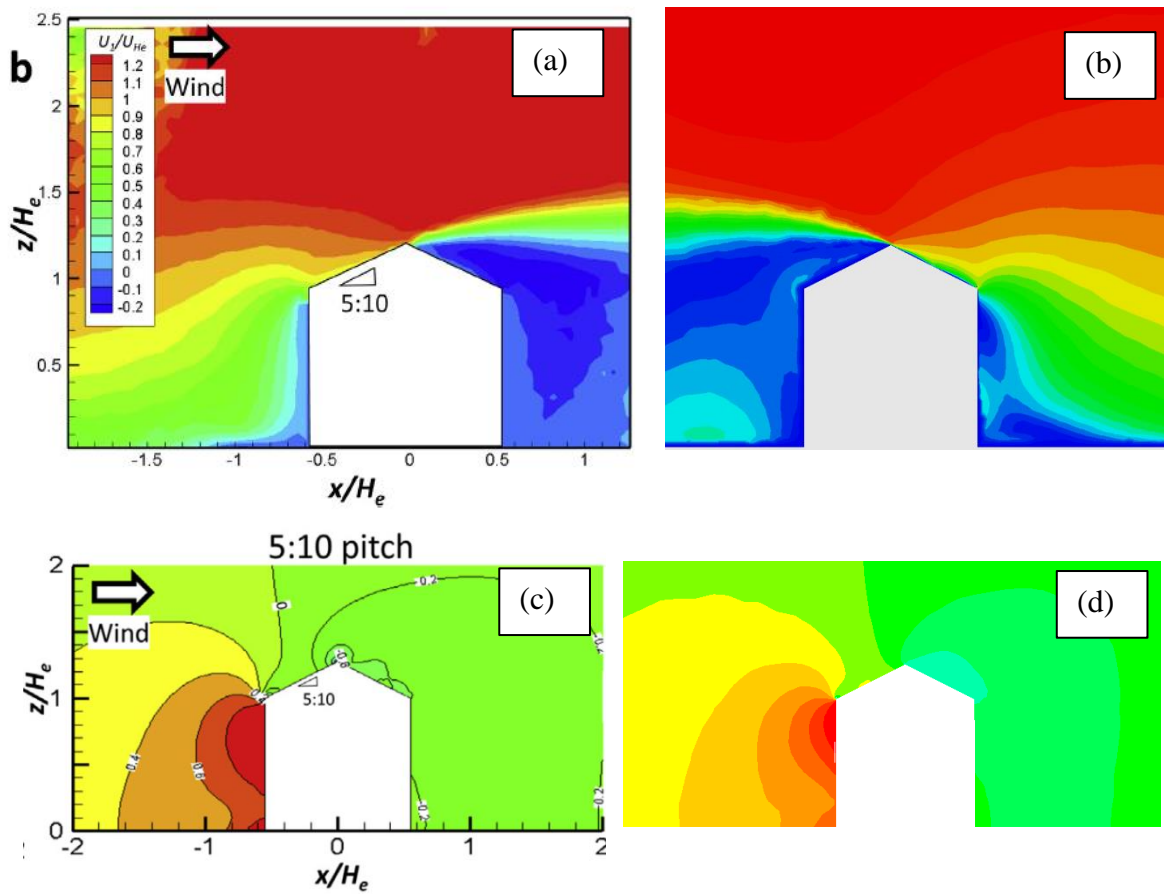


Fig. 28. (a) PIV measurements of velocity [51] (b) velocity distribution in the current model (c) pressure coefficient result [51] (d) pressure coefficient distribution in the current model.

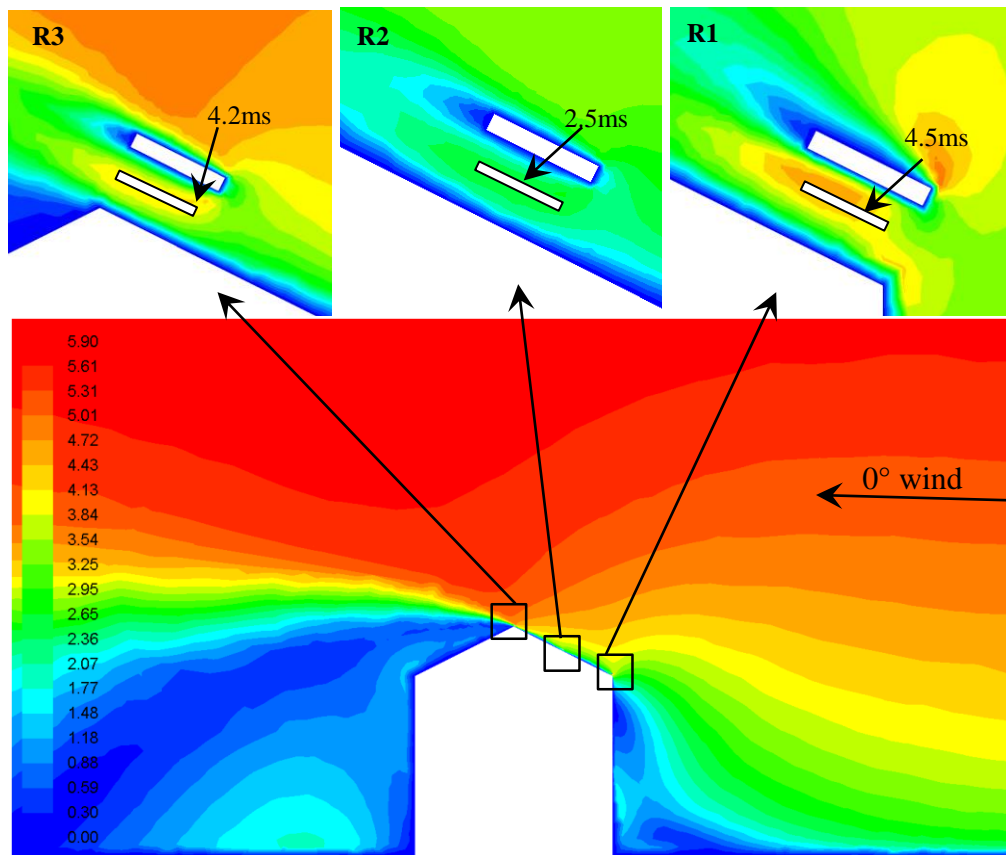


Fig. 29. Contours of velocity magnitude showing a cross-sectional side view of the building

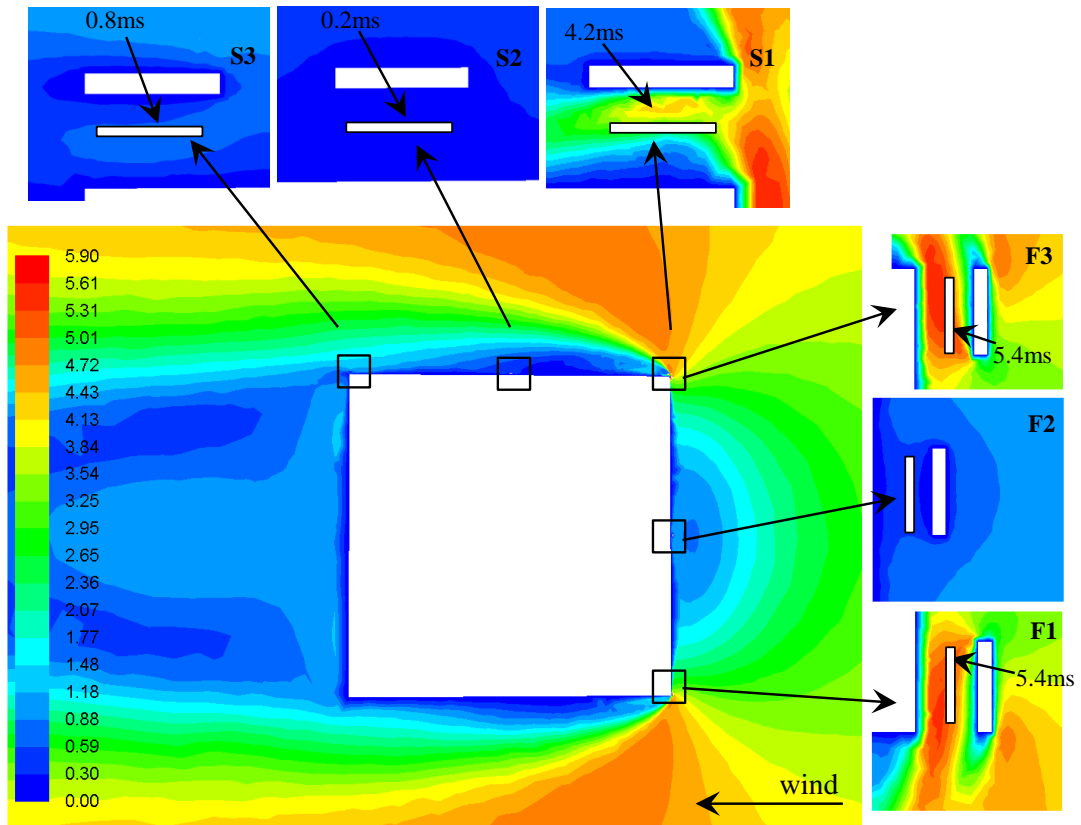


Fig. 30. Contours of velocity magnitude showing a cross-sectional top view of the building

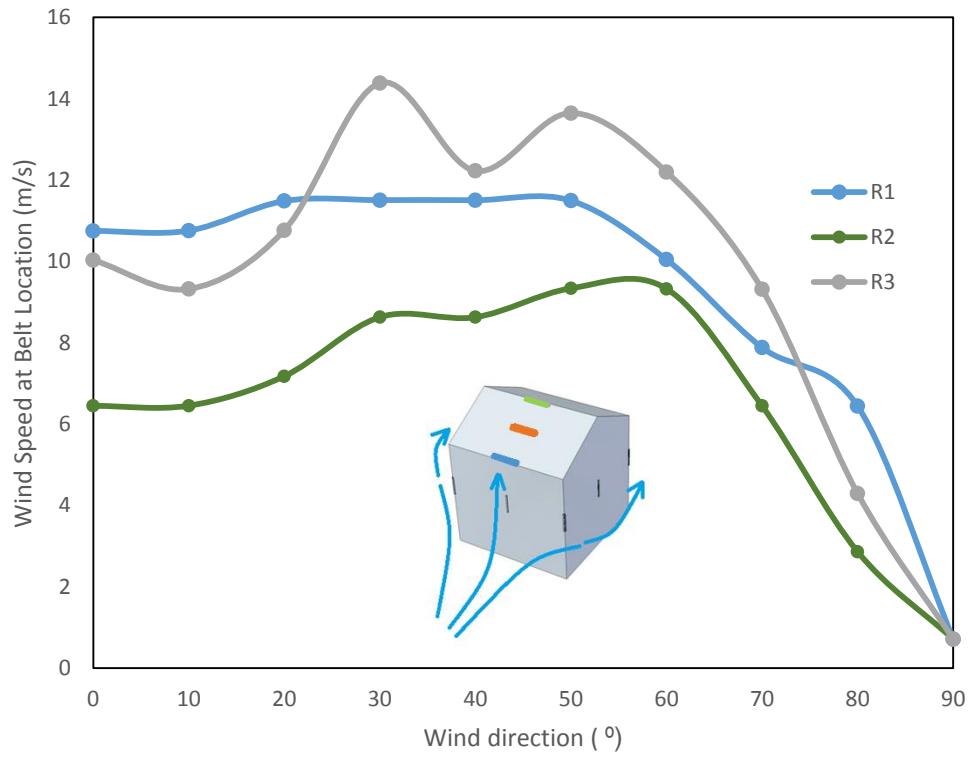


Fig. 31. Effect of wind direction on the wind speed at belt located on the roof for various wind angle of approach with outdoor wind  $U_H = 10$  m/s.

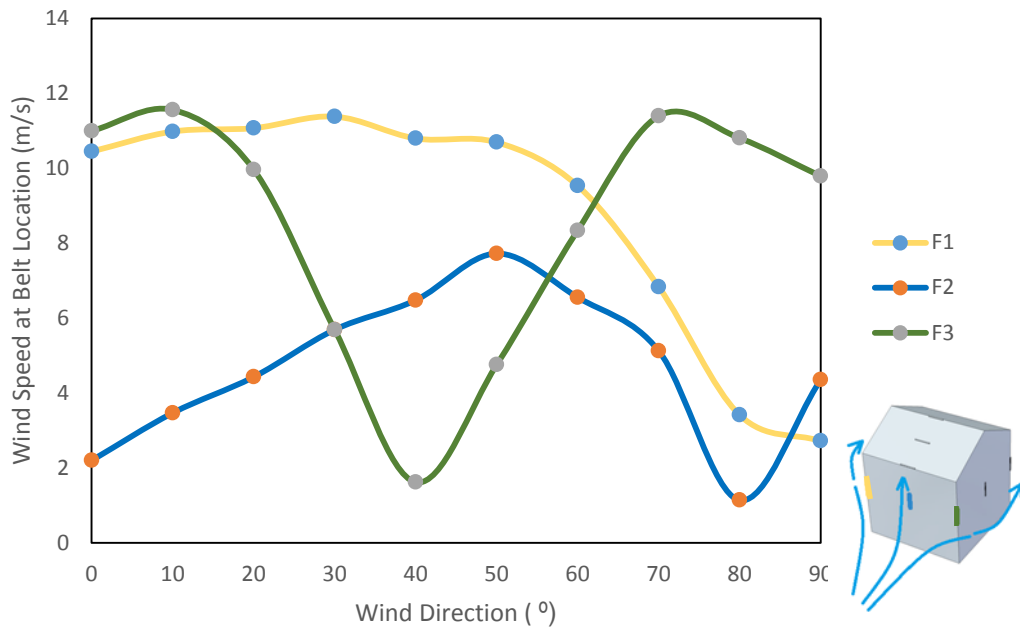


Fig. 32. Effect of wind direction on the wind speed at belt located on the windward side of building with outdoor wind at  $U_H = 10$  m/s

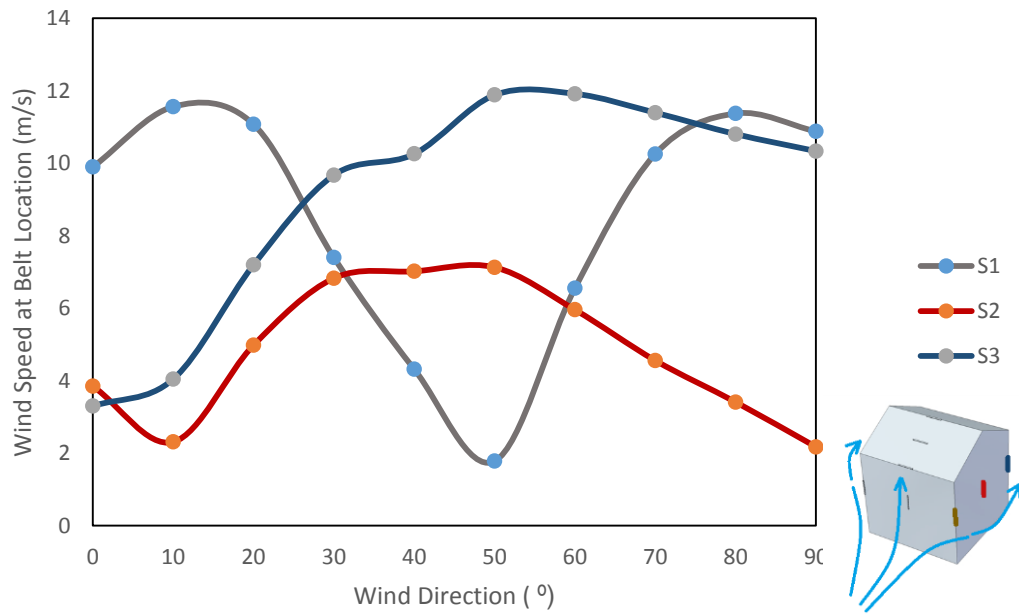


Fig. 33. Effect of wind direction on the wind speed at belt located on the side of building with outdoor wind at  $U_H = 10$  m/s

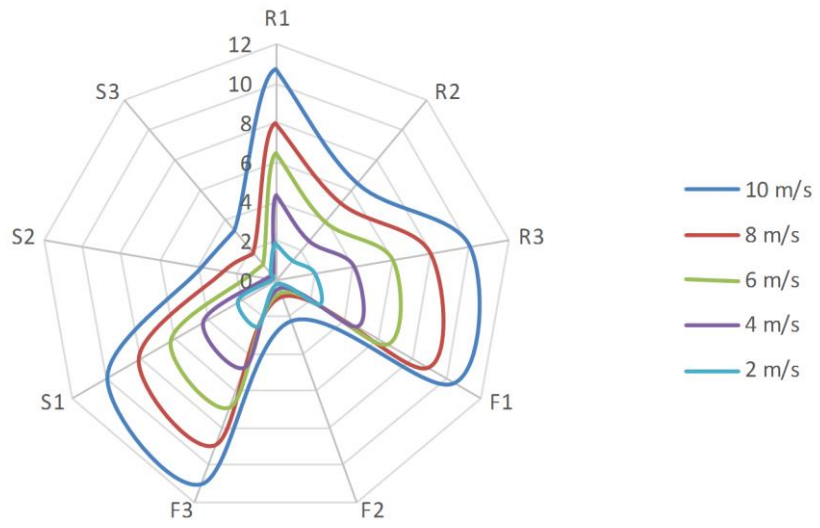


Fig. 34. Wind speeds gathered at belt position for various mounting locations for 0° wind angle of approach

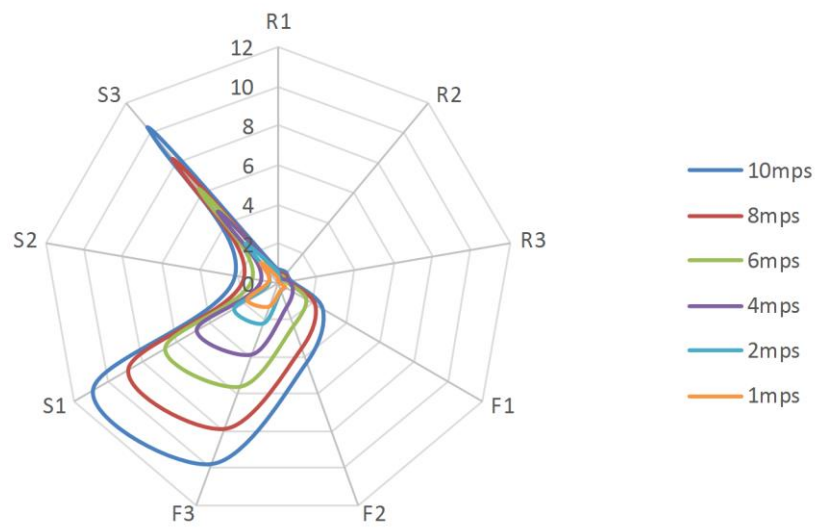


Fig. 35. Wind speeds gathered at belt position for various mounting locations for 90° wind angle of approach

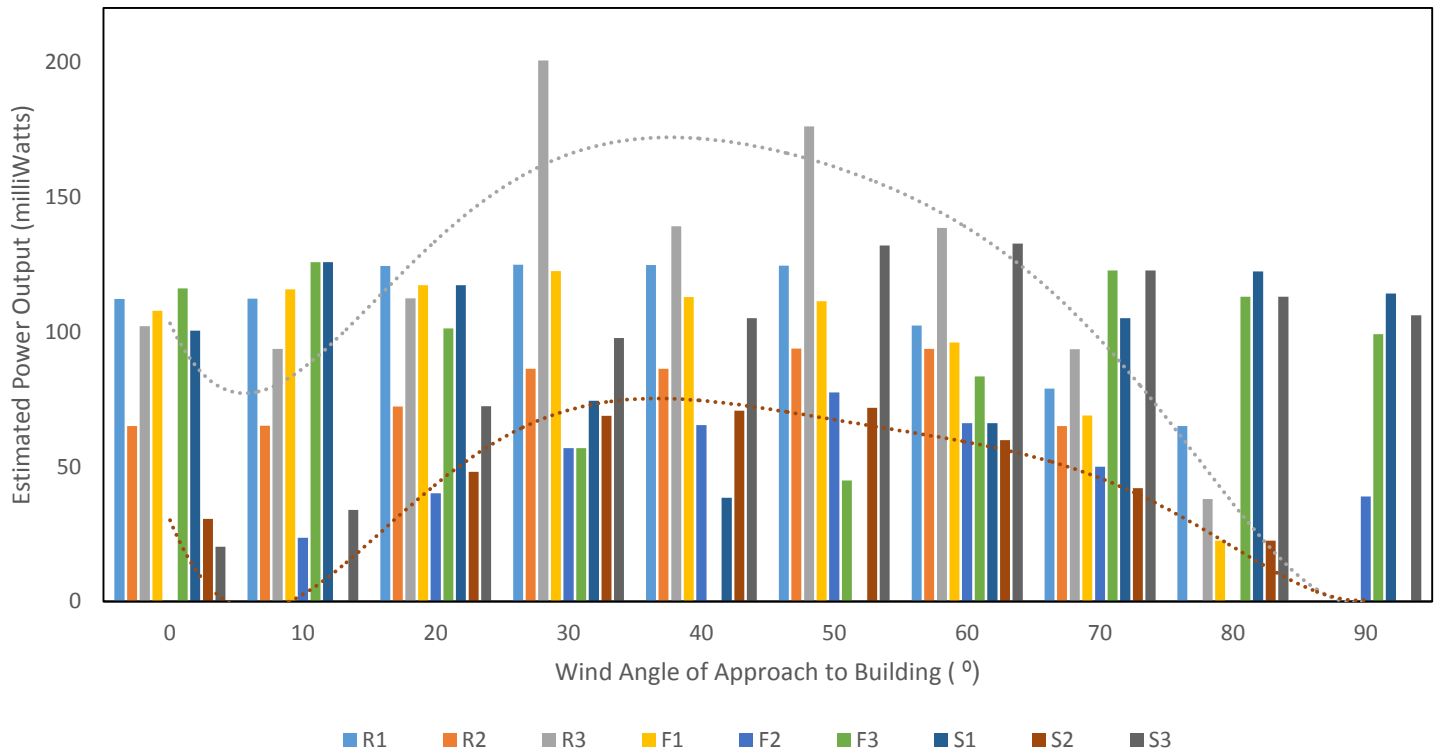


Fig. 36. Sample calculation based on aero-elastic belt (2-magnet-coil system) data measured from experimental data [6] showing the trend lines for R3 (green) and S2 (maroon)

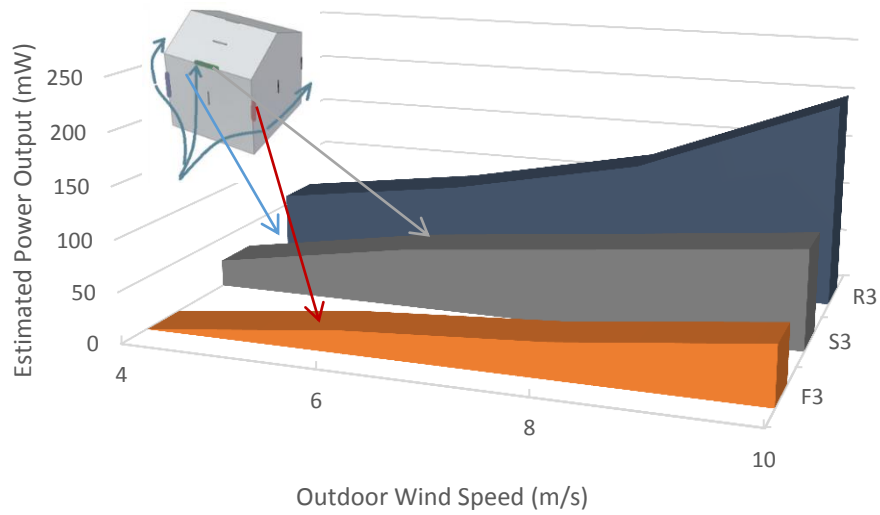


Fig. 37. Impact of various outdoor wind speeds ( $U_H$ ) on the estimated output of the aero-elastic belt for locations F3, S3 and R3

Table 1. Summary of the CFD model boundary conditions.

Summary of the CFD model boundary conditions.	
Boundary condition	Set value
Algorithm	SIMPLE
Time	Steady state
Solver type	Pressure based
Discretisation Scheme	Second order upwind
Turbulence model	Standard k-epsilon
Near wall	Standard wall functions
Velocity inlet	ABL profile (see Fig. 27)
Pressure outlet	0 Pa